SECOND COPY

Radio Frequency Properties of Melt-Recrystallized $YBa_2Cu_3O_{7-\delta}$ Fibers

by
Michael W. Daniels
B.S. Materials Science and Engineering
Massachusetts Institute of Technology, 1993

Submitted to the Materials Science and Engineering Department
in Partial Fulfillment of the Requirements for the Degree of
Master of Science
in Materials Science and Engineering

at the
Massachusetts Institute of Technology

May 1994

Signature of Author.....
Department of Materials Science and Engineering
May 6, 1994

Certified by.....
Michael J. Cima
Professor in Materials Science and Engineering
Thesis Supervisor

Accepted by.....
Carl V. Thompson II
Professor of Electronic Materials
Chair, Departmental Committee on Graduate Students

Radio Frequency Properties of Melt-Recrystallized
$YBa_2Cu_3O_{7-\delta}$ Fibers

by
Michael W. Daniels

Submitted to the Materials Science and Engineering Department
on May 6, 1994 in partial fulfillment of the requirements for the degree of
Master of Science in Materials Science and Engineering

Abstract

$YBa_2Cu_3O_{7-\delta}$ (YBCO) is investigated as a substitute for copper in a resonating cavity antenna. Melt-recrystallization is used to produce fibers with dense, long-grained material, in an attempt to minimize power losses in the antenna. Optical microscopy on fibers processed in this manner revealed several features, including a second phase at platelet boundaries. SEM revealed a surface coating that increased the surface resistance of the fiber. Electrical measurements revealed surface resistances around 10^{-3} to 10^{-4} Ω. The surface resistance increased with frequency and applied magnetic field power. The field dependence was linear, suggesting weak-link dominated behavior. The surface resistance appeared to taper off at higher powers, indicating the magnetic powers used may be near saturation for the samples. A rough correlation was also found between the grain size of the sample and its surface resistance. The best surface resistances achieved were still two orders of magnitude higher than that of thin film stripline samples of other studies. However, the YBCO fibers generally had lower surface resistances than copper, making them valid replacements for copper.

Thesis Supervisor: Dr. Michael J. Cima
Title: Professor of Materials Science and Engineering

Dedication

I dedicate this thesis to my Koon-Yai, to whom I owe the past five years of my schooling. She believed in having the best education possible, and worked hard to give it to me

Acknowledgments

I wish to thank Dr. Mark Parish and David Chandler for their expertise and help. I am greatly indebted to Charlie Cary for the electrical testing, and to CeraNova Corporation for supporting my work.

.

Table of Contents

List of Tables

List of Figures

I. Introduction

Superconductors have many potential applications, but one with enormous potential is for use in antennas. A superconducting antenna would allow transmission of far more powerful signals with fewer power losses from ohmic resistance existing in normal materials. The advantage of a superconducting antenna becomes more evident when one considers a potential antenna design consisting of a helical coil inside a resonating cavity [13,14]. This design achieves the same frequencies as much larger antennas, but in a much smaller space. As an example [13], the frequency of a 25 feet coaxial resonating antenna three inches in diameter can be achieved by a helical resonating antenna 8" long and 6" in diameter. Such an antenna would be much more mobile, allowing a wide range of new applications. This favorable size comes at the price of having a much greater power loss in the smaller surface of the center conductor. High power transmission applications using conventional materials like copper become impractical for this design because the resistance is too high.

The advent of high temperature superconductors allows one to achieve the potential of this antenna design for radio frequency applications. The focus of this research is to develop the processing of $YBa_2Cu_3O_{7-\delta}$ (YBCO) superconductor for the antenna application. Most applications for bulk superconductors, such as for transmission lines or motor coils, focus efforts on improvement of critical current by control of microstructure. However, the use YBCO as an antenna for radio transmission creates its own unique set of electrical requirements for the superconductor.

The current direction rapidly switches many times a second in radio frequency (rf) applications. This produces several effects not present in normal DC applications. One of the main effects is the skin depth effect, where current flow is restricted to the surface. The cause of this physical phenomenon lies not in the nature of the superconducting material, but occurs in all conductors when used at radio frequencies. As an electromagnetic wave penetrates a conductor, the electric field causes electrons at the surface to move in response. The wave decays as it passes into the conductor. The thickness of material that the wave penetrates before decaying to 1/e of its value, the skin depth, is proportional to $\omega^{-1/2}$ where ω is the frequency [29]. Most of the current will be carried within the skin depth. As a result, the surface resistance is dependent on frequency. This type of decay occurs in both normal conductors and superconductors, and occurs whether the conductor is receiving an incoming wave or transmitting one.

Another difference between rf applications and DC applications is the mechanisms that reduce the electrical performance. There are losses inherent in the superconducting nature of materials, which arise from the existence of normal electrons in all superconductors above 0 K. Also, magnetic flux movement and penetration at the grain boundaries cause power losses, so it becomes even more crucial to have a

high density of magnetic flux pinning sites. Weak-link behavior at the grain boundaries also contribute to losses, so grain boundaries should be minimized by maximizing grain size.

The importance of the microstructure of the YBCO conductor becomes apparent for antennas. For this reason, melt-processing techniques will be used to produce high quality bulk material with long grain lengths. The YBCO material is ultimately intended to replace the center helical coil in a helical resonator. Techniques for melt-processing the coil shape have yet to be developed. Meanwhile, the microstructural improvement on antenna performance will first be examined by using simpler, straight fibers as the center conductor. Fibers will be melt-recrystallized by a simple zone-melting furnace. This study will focus on the relationship between the microstructural properties and antenna performance of the fiber. The fibers will be melt-recrystallized under a range of growth conditions and the resulting microstructure will be examined for the purposes of improving the process to fabricate better material to improve antenna performance.

II. Background

A. Magnetic Flux Pinning

In type II superconductors, such as YBCO, magnetic flux is able to penetrate the material through the normal regions [1]. Fluxoids develop in the superconductor surrounding the flux lines. The tendency is for Lorentz forces to move the fluxoids when there is transport current flowing through the material. Pinning sites help prevent the motion of the fluxoids. If the force on the fluxoids exceeds the pinning force, they move through the material. The viscous-like drag caused by the pinning sites requires work to keep the flux moving, resulting in a voltage drop across the superconductor. Pinning sites are small regions of disorder where the material is not superconducting. This normal region is energetically favored by a fluxoid, so the fluxoid tends to sit at the site, and needs to overcome an energy barrier to move off the normal region. The pinning site should be smaller than the coherence length, which reflects the distance over which the normal material to superconducting material transition occurs. For YBCO, this length is 7-34 Å, depending on the crystallographic direction of the current [11]. This very short coherence results in a variety of effects uncommon in low-temperature superconductors, such as weak link behavior.

One type of defect is the twinning planes, which form from the anisotropic shrinkage during the tetragonal to orthorhombic phase transition around 670 °C. The best superconduction properties are achieved in fully oxygenated 123 phase. Material that is properly oxygenated goes through the tetragonal to orthorhombic transition. Material that does not make the phase transition remains a non-superconducting

tetragonal phase at room temperature. A high degree of twinning is a good indication of a high amount of superconducting material. The twinning planes are of the appropriate size to pin flux, but are shown to be weak pinning sites[18]. A more effective pinning site is a stacking fault, which is shown to be more numerous around 211 phase inclusions[18]. As would be expected, a high surface to volume ratio of 211 in bulk YBCO gives better flux pinning [21], due to the larger proportion of stacking faults.

The fluxoids tend to set up in an elastic lattice [1], so that a group of fluxoids, called a "flux bundle," may be held fixed as a group by a few strong sites, and it is not necessary to pin each fluxoid individually. As the current flows, the magnetic flux bundle drifts until it is arrested by a sufficient number of pinning sites. When the current switches direction, the flux drifts in the opposite direction, so the pinning sites which initially held the flux may now be on the wrong side to effectively hold it. The flux continues to drift in the other direction until it runs up against enough pinning sites to hold it. As the current switches back and forth, the flux drifts back and forth between the pinning sites. A high density of effective pinning sites is required to limit the amount of the back and forth flux drift, which saps the antenna transmission power. The higher the transmission power used for the application, the stronger will be the flux motion. This is another reason for the need of a high density of strong pinning sites.

B. Power Loss

Power loss is the amount of signal power lost in the conductor without getting transmitted. The power loss often takes the form of heat in the conductor, which worsens the properties in superconductors by the temperature rise. There are intrinsic and extrinsic reasons for power loss. Intrinsic losses result from limits in the nature of superconducting materials. Extrinsic losses are believed to result from weak links present in the material, such as at grain boundaries. The essential features of the some proposed models to explain intrinsic and extrinsic behavior are discussed below.

Intrinsic power loss is due to resistive current flow that can exist in a superconductor when an AC field is applied [1]. This type of current flow is a result of the rapid switching back and forth of the superconduction current. There is a fraction of non-superconducting normal electrons in any superconductor above 0 K. During DC flow, the current is carried exclusively by the superconducting electrons, so there is no resistance. When AC flow occurs, however, the changing field must accelerate the electrons in the direction of the electric field. This is not instantaneous, since there is a small momentum associated with the electrons, and the superconducting current lags behind the AC field. A small voltage to accelerate the superconducting electrons must exist. This voltage can also move normal electrons, so that in an AC field the current is carried by both ohmic normal electrons and by superconducting electrons. This is

known as the "two fluid model". The normal electron current creates a power loss by its ohmic resistance in a superconductor.

Extrinsic power losses can arise from weak-link Josephson junctions at grain boundaries. Magnetic flux decays exponentially along the penetration depth into the material. Above a critical field, magnetic flux is able to penetrate through the weak-link grain boundaries at the surface [24]. Flux penetration deep into the material at the grain boundaries can result in more losses as it gives rise to current into the grains and across the grain boundaries. Flux pinning limits this deleterious penetration by pinning the current into the grains and at grain boundaries.

The power losses result from the surface resistance (R_s) of the conductor. The surface resistance is the resistance to current flowing within a certain skin depth of the material. The R_s is measured in a resonator with YBCO as one of the conductors. The measurement used to gauge the conductor performance was the Q, a dimensionless number indicating the antenna performance in the cavity. The Q is measured from the peak width at half the peak height of the reflected power near the resonating frequency. A high Q means low losses at the resonant frequency of the cavity. The cavity used consists of a cylindrical chamber with a center conductor. This center conductor was replaced with a superconducting fiber. The Q depends on the geometry and the electrical properties of the cavity, but more importantly it is also a function of the fiber conductor in the center. The greater the power losses in the fiber, the lower the Q. The surface resistance can be defined from the quality factor, Q, according to the following equation [17]:

$$R_s \equiv \Gamma f / Q$$

where Γ is a geometrical factor, and f is the frequency. This R_s is only an effective surface resistance value, since the real surface resistance varies with position along the fiber. This variation arises from the nature of the standing wave in the cavity, where the current and penetration depth will be highest at the antinodes.

The R_s in YBCO is found to increase with frequency (ω) and the power applied. The surface resistance has generally been shown to vary with the square of the frequency [17]. A study with sintered rods [24] shows an R_s dependence with $\omega^{1/2}$ at high powers. This is also the type of dependence a normal conductor has. These dependences are predicted by a variety of models, including a two-fluid model and other models based on grain boundary weak links.

The power reflection from the cavity will peak at a resonant frequency, as power is applied to the cavity. This peak plotted versus frequency has a slight asymmetry in superconductors, that is absent in normal conductors. This non-linearity can be explained using the two-fluid model, and matches well with experimental values for thin film YBCO[16]. The implication of this model is a slight shift in the resonant

frequency with applied power, and a power loss dependence on frequency. Though the frequency dependence was not studied in depth for this thesis, one should be aware how the frequency chosen affects the R_s, and possibly influences the dominant mechanism of power dissipation.

The surface resistance for normal conductors is independent of the power level applied. However, YBCO and other superconductors have higher surface resistances with higher power levels. The power dependence determines how effective the antenna will be when used to transmit powerful signals, and what the maximum transmission signal can be. The power applied is represented by the radio frequency magnetic field (H_{rf}) at the surface of the conductor. This allows comparison of different superconductor specimens, even though they may have been tested in different types of resonators. The R_s dependence on H_{rf} depends very much on the materials properties and the particular test parameters.

The two-fluid model can be used to show a quadratic dependence of R_s on H_{rf} [17]. The higher the power used, the more conduction that will occur by normal electrons. A different model proposed by Halbritter[30] predicts a linear R_s dependence on power by assuming that weak-link Josephson junctions at the grain boundaries dominate the dissipation behavior. Flux is able to penetrate deeper into the material along a weak-link grain boundary. The model gives a fairly linear R_s dependence with low power, due to flux penetration at the grain boundaries. It gives a very non-linear dependence at high H_{rf}, which results in an asymmetric resonance curve. The R_s saturates at high H_{rf} when high frequencies are used.

Energy gap considerations are important at frequencies approaching 1 THz [29], but do not apply to this thesis since the effect is not dominant at high temperatures near T_c, and the frequencies used in this study will be much lower.

The results of a number of bulk and thin film studies [24] suggest a quadratic dependence on H_{rf} at low powers, and a linear dependence at intermediate powers (0.1 to 10 Oe). The R_s saturated when the power applied was above a critical power, which ranged from 10 Oe to 100 Oe depending on the sample and conditions used. These dependences are supported by results found in Oates, et al [17]. A summary of the surface resistances measured in various materials at 4.2K are shown in Figure 1.

Studies with stripline resonators [28] using thin films also show a quadratic dependence at very low powers, in which it is believed the dependence to be a result of defects and very weak links in YBCO. The power dependence at moderately low powers followed the quadratic relation:

$$R_s = R_{so}(1 + b_{rf}H_{rf}^2)$$

where b_{rf} is a fitting constant. This dependence may rise from weak-link Josephson junctions at the grain boundaries. The R_s dependence on H_{rf} was even greater at

medium powers. The flux penetration at the grain boundaries becomes significant at high powers, and hysteresis losses play a role in power dissipation.

A linear dependence of R_s has been found in relatively poor thin film samples with many grain boundaries, and follows the relation [17]:

$$R_s = R_{so}(1 + \beta H_{rf})$$

where β is a fitting constant. The linear dependence is associated with Josephson junctions at weak-links at the grain boundaries, where magnetic flux is able to penetrate.

The quality of the conducting material has been shown to affect the R_s. For example, studies measuring the R_s of polycrystalline YBCO and its dependence on field and temperature, give a values of $1x10^{-4}$ to $8x10^{-4}$ Ω at 1 GHz, 77K and low applied fields [5,30,34]. The surface resistance of a thin film in a strip line resonator is better, at $2x10^{-6}$ to $8x10^{-6}$ Ω [17,30,35]. The thin film values represent good quality material with few grain boundaries and good pinning defects, and therefore indicate the potential which may be achieved in bulk materials given sufficient microstructure control.

Increasing the grain size and improving the alignment by texturing reduces the R_s [24]. An untextured film had a higher R_s which increased faster with H_{rf} than the R_s for a textured film. The microstructure was also shown to affect the R_s dependence in stripline resonators [28]. Poorer films in stripline resonators showed a linear R_s dependence on H_{rf}, which may be due to flux penetration at grain boundaries.

Studies can be done to examine how different defects affect the power loss, since flux pinning affects the power loss. Twinning defects have been shown to pin flux flow [26], by applying an external magnetic field at different orientations to a crystallographically oriented sample. These results fit with simulations of power loss due to flux flow response to applied power.

C. Microstructure

Improvements for YBCO conductor as an "rf" were studied by improving the microstructure. Longer, well-oriented grains and cleaner grain boundaries can be achieved through melt-processing [20]. Straight fibers were used in this study because of their simple but useful shape and ease of melt-processing.

A variety of melt-processing techniques are available [20]. The process used in this study is a melt-recrystallization process in a resistive zone furnace. This method melts a small section of the material in a hot zone. A peritectic melt forms from YBCO, consisting of Y_2BaCuO_5 (211) particles and a Ba and Cu rich liquid phase.

The material passes through this melt zone, and the exiting liquid reacts with the 211 to solidify as 123 phase at a crystal growth front. This growth front can theoretically continue indefinitely under appropriate growth conditions, resulting in a single grain over the entire material. An excess of 20% vol 211 is used for this process, so that there is sure to be enough solid material remaining above the peritectic melting temperature to hold the length of fiber suspended below the melt. The size of the 211 after melt-recrystallization is influenced by the initial size of the material and the amount of coarsening that took place in the melt.

The fast growth direction of 123 is along its a-b plane. This results in a high degree of orientation in the processed fiber, with the a-b plane aligned along the growth direction. This is fortunate for zone melting of a fiber, since the material's anisotropic conductivity favors conduction along the a-b plane, which generally lies in the long axis of the fiber. The anisotropic growth rate also results in a thin platelet structure. The grain consists of long platelets oriented along the a-b plane. The individual platelets are not separate grains, but instead are interconnected at various points along the platelets. This will be discussed further in the Discussion section.

The conditions of growth have a large effect on microstructure [9] due to compositional segregation at the solidification front. The sharpness of the thermal gradient and the growth speed are the two most important factors to controlling the growth front. A thermal gradient too low or a growth speed too high results in dendritic or cellular growth. In such a case, the resulting material consists of many fine grains oriented roughly along the axis. In extreme cases the grains can nucleate ahead of the growth front, resulting in a fine-grained randomly oriented microstructure. For obtaining quality melt-recrystallized YBCO fibers, growth conditions must be chosen to achieve a stable, single grain growth front.

III. Experiment

A flowchart summary of the basic steps performed with the fiber material are illustrated in the Appendix.

A. Zone Melting

The starting material was made from YBCO powder purchased from Rolm-Pulanc, mixed with an excess of 20% vol 211 powder. Through a CeraNova Corporation proprietary process, the powder was mixed with 50% binder and lubricant, and then extruded into a 10 mil green fiber. The fiber was heat-treated to remove the

binder and sintered at 890 °C for 1 hour. This gave straight fibers roughly 200 μm in diameter and in lengths over 30 cm long.

The sintered material was melt recrystallized in an electrically heated zone-melting furnace in air. This furnace was essentially a vertical tube furnace with a 3/8" to ¼" inner diameter [Figure 2]. A heater coil was placed around the middle section of the furnace, where the tube was cut away to allow direct heat from the coil to a YBCO fiber in the center. The temperature was controlled by a thermocouple near the heating coils. There are many factors affecting the vertical temperature profile in the furnace, including the shape and size of the coils, distance from the coils to the fiber, inner diameter of the furnace, and the thermal conductivity of the materials used for the tube. Hence, though all the furnaces are essentially the same, differences between the furnaces due to the construction affect the thermal gradient, temperature profile, length of the hot zone, and the uniformity of azimuthal thermal gradient. In each of the four furnaces used, the fiber was suspended in the furnace from a supporting filament that was wound around a pulley attached to a very slow speed motor. This setup allowed the fiber to be drawn through the furnace at speeds ranging from 1.6 mm/hr to 9.9 mm/hr in either direction.

Estimates of the temperature profiles were measured by passing type K thermocouple (0.005" diameter) through the zone furnace at 3.3 mm/hr while the furnace set point temperature was 1010 °C, typical conditions used for melt-recrystallization. The resulting temperature profile for each furnace was recorded by a chart recorder. The profiles reflect the temperature near the center of the furnace, not the temperature at the furnace thermocouple used to control the furnace temperature.

Experiments were carried out in each furnace to determine the microstructural features formed in the initial melt zone. This involved placing a sintered fiber in the furnace center at 750 °C and ramping to the set point temperature, 1010 °C, over 15 minutes. This ramp was the same ramp used for melt-recrystallization of the fiber in all other experiments. The ramp was needed to allow the section to slowly reach its melt temperature under stable conditions, instead of being rapidly dropped into hot zone, which often resulted in one side of the fiber melting first and giving a kink or slight bow in the fiber. After the ramp, the sample was held in place 1 hour at a set point of 1010 °C, and then air quenched to room temperature. The resulting features were examined and measured using optical polarized microscopy.

The sintered fiber could be drawn in either direction through the furnace at a variety of growth speeds and temperatures. To determine the effect of these, several experiments were performed under a variety of conditions [Table 1]. These conditions were chosen based on previous work at CeraNova, which showed melting of the fiber to occur above a set temperature of 1000 °C, while single crystal growth generally occurred at growth speeds at or below 5.0 mm/hr.

The fibers were annealed, after melt-recrystallization, in an environment containing 1 atm flowing oxygen. The anneal cycle consisted of a ramp to 880 °C for sintering of silver lead attachments (to be described below), and then cooled to 670 °C, where the tetragonal to orthorhombic transition occurs. The fibers were then slowly cooled to 450 °C and soaked for 40 hours before being slowly cooled to 350 °C where it would also soak for 15 hours before being cooled to room temperature. Indication of the success of the anneal can be observed in the amount of twinning in polished samples.

The fibers were then mounted in epoxy and carefully ground to reveal the cross-section along the length. After polishing, they were examined by polarized optical microscopy to determine the lengths of various features and to try to quantify the quality of the microstructure.

The grain length was taken by dividing the length of a selected section by the number of intersections of grain boundaries intersecting the fiber edge on the polished cross-section. This technique was used because it only counts the number of grain boundaries actually reaching the surface of the sample, which controls the power losses.

Parts of a few melt-recrystallized samples were examined by SEM to examine the fiber surface and the surface of the fractured ends.

B. RF Testing

RF testing was done in a half-wave coaxial resonating cavity constructed out of copper [Figure 3]. The cavity consisted of a 6" long copper cylinder 3" in diameter. Copper endcaps placed over the ends of the cylinder made up the endwalls of the cavity. Coaxial cable connections in the endcaps connected external cables to copper wire electrodes. The endcaps could slide in or out to adjust for different sample lengths. Shorter cylinders were used for fibers significantly shorter than 6".

This setup achieves high fields at the conductor surface because a large amount of power is concentrated at the relatively small surface of the thin fiber. Another existing method to measure surface resistance in a resonating cavity involves replacing the endwall with the YBCO sample, which allows one to use flat samples. However, this has the disadvantage that the entire cavity must coated with superconducting material, or otherwise the cavity losses will overwhelm the signal. Center conductor replacement can be done in a copper walled cavity [25]. The copper cavity used in this thesis was able to measure samples with a Q as high as 30,000 before cavity losses would begin to significantly affect the measurements.

The center conductor YBCO fiber was placed in a sapphire tube for ease of handling. Sapphire was used because of its low dielectric loss, which does not significantly affect the measured Q. All testing was done in liquid nitrogen at 77 K.

A variety of methods were used to connect the fiber ends to the electrodes of the cavity. One method involved attaching silver leads by silver paint, and then heating up to 880 °C to sinter the silver, before ramping down to 670 °C where the anneal cycle would start. Another approach was to remove the wires, but leave the sintered silver ends, and having the fiber be capacitively coupled to the electrodes. A third approach was to simply leave out the silver entirely and to leave the ends capacitively coupled to the electrodes. The silver was found to reduce the Q, so it was removed for all tests.

Power was supplied to the cavity and analyzed by a Hewlett-Packard 8753C Network Analyzer. The Q is affected by losses in the external cables and connections to the cavities. These losses are minimized by increasing the capacitive spacing between the electrodes and the YBCO conductor, which decouples the electrodes from the conductor, and so fewer losses exist in the external lines. These losses can not be completely eliminated, otherwise the signal becomes too small, and so the Q must still be corrected, as will be described later.

The samples were measured at the resonant frequency, which depends on the physical geometry of the cavity and sample. This frequency was typically around 1000 MHz for a 10 cm sample, and 700-800 MHz for the 15 cm samples. The Q was measured for a range of source powers, from -10 dBm to 20 dBm.

The R_s can be determined by measuring the Q of a copper conductor and relating it to YBCO by analysis described in [25]. The power at the conductor surface is calculated from the source power, Q, conductor geometry and various other parameters [28]. These calculations are described in the Appendix.

IV. Results and Discussion

A. Processing and Microstructure

General Features

The temperature profiles of each of the furnaces are shown in Figure 4. These profiles show a peak temperature 30-70 °C higher than the set temperature used to control the furnace. This is expected, since the control thermocouple could not be placed in the hottest part of the furnace, i.e. the center of it where the fiber was. These measured profiles are only rough estimates of the actual temperatures, since the thermocouple wire has different conductive and emissivity coefficients than a YBCO

fiber. However, the profiles roughly correlate with the melt zone lengths found in the melt-zone length experiments and other measurements. Furnaces #1, #2, and #4 were roughly the same, with similar hot zone lengths and thermal gradients at the growth front. Furnace #3 had a hot zone length roughly double that of the other furnaces, and had a shallow thermal gradient. These differences are due to deliberate construction differences in the furnace to see what effect a different temperature profile might have on the processing of the samples.

The one hour hold experiments showed the same bloat features found in the melt-recrystallized samples. The quenched melt zone consisted of fine polygrained material. There were pores and pullouts. The pullout material is likely to be agglomerates of 211, of which there is a large amount in the peritectic melt. The melt zone is shorter than the length of the melt zone found after zone-melting for several days. The increase in melt zone length after one day is typically 35-40%. This is not surprising, since the hot zone is expected to expand over long times as the entire furnace gradually heats up to its equilibrium state.

The melt-recrystallization process produced a series of microstructural features in the melt-recrystallized specimens. There is a bloat zone at the beginning of the process that is larger in diameter than the sintered material [Figure 5]. This bloat zone forms when the liquid wicks from the melt zone into the adjacent porous sintered material. The excess liquid adds to the material and causes it to be bloated. The liquid wicks away until it reaches a front that is cool enough to solidify it. The bloat zone beneath the melt zone sometimes has a bell-shape, and appears as if sagging [Figure 6]. There were differences in the bloat zone lengths depending on which furnace was used. The essential difference between each furnace is its temperature profile. The distance at which the solidification for this liquid phase occurs is dependent on the temperature profile. By correlating the bloat zone length and the temperature profiles of the furnaces, the temperature where the bloat zone ends is found to range from 900 °C to 925 °C [Figure 4]. This is the solidification temperature of the wicking liquid phase. The exit bloat zone is defined as the bloat zone which starts out on the exiting end of the furnace and moves away from the hot zone without getting melt-recrystallized. There is a similar bloat zone on the other side of the melt zone, which is referred to as the feed bloat zone, since it feeds into the melt zone during the zone-melting process.

The area next to the bloat zone is the melt zone, over which the material is a peritectic liquid mixed with 211 phase material. The initial melt zone exhibits the cleanest microstructure of the entire sample, having few pores, second phase pullouts, or any other features aside from 211 particles and 123 phase. This material is much richer in 211 particles, since the Ba-Cu rich liquid has wicked from this zone into the adjacent bloat zones. The 211 particles are usually large and spherical, and after solidification occupy more than 1/2 of the volume, based on visual estimates. The volume fraction of 211 will naturally be even higher when above the peritectic melt. The fiber diameter is thinner in this region, due to the loss of liquid and porosity. The

211 particles shrink closer together as the liquid leaves, and the fiber length actually decreases at this point.

Initially, this melt-zone solidifies to form multiple unaligned grains around 0.2 mm in size. The grains with a favorable orientation aligned along the growth direction quickly crowd out the other randomly oriented grains that grow slower in this direction. A single grain aligned along the growth direction quickly crowds out the other grains. The growth is fastest in the a-b plane, so the single grain will be oriented such that this plane is aligned along the growth axis. This grain typically continues 5-20 mm before it is replaced by another grain. The subsequent grains after the initial single grain are usually smaller and more randomly oriented, and rarely achieve a length comparable to the initial grain.

The first single grain rarely passed beyond the boundary determined by the edge of the initial melt zone. This boundary is distinguished by a slight increase in diameter of the fiber. This occurs because the initial melt zone is thinner from its loss of liquid, but the subsequent region the melt zone encounters, the feed bloat zone, is already bloated, and so the fiber will be fatter. This material entering the melt zone from the feed bloat zone is rich in the liquid phase, and poorer in the 211 phase. As this material melts above the peritectic, the excess liquid again attempts to wick away into the neighboring area, except that this time instead of the porous region at the exit end, the melt runs into a dense, melt-recrystallized region that can not absorb any liquid. It is expected that some of this peritectic liquid and accompanying 211 phase drips down the sides, along the surface of the melt-recrystallized region. Some liquid is able to continue to wick ahead into the feed bloat zone. The leading edge of the feed bloat zone, the edge furthest from the melt zone, will continue to advance as the hot zone moves along the fiber. The feed bloat zone keeps advancing, while its trailing edge gets consumed by the advancing melt zone. A steady state is reached, and there is not a net loss of liquid from the melt zone from then on. The fiber resumes a constant diameter, while the bloat zone dimensions also stay constant except for the slight lengthening due to the furnace reaching an equilibrium temperature profile.

There is rarely another grain of comparable length after the initial long grain ends. It is not clear what prevents the grain from continuing to longer lengths. The growth speeds are appropriate for single grain growth in the thermal gradient used. Since the results did not appear to be affected within the range of growth speeds used, the problem is expected to lie elsewhere.

One likely reason for truncated grain growth lies in the geometry of the hot zone. Some samples showed a series of grains, each starting from one side and then slanting across the fiber [Figure 7]. This is believed to be an indication of an uneven azimuthal temperature gradient. If the furnace is hotter on one side of the fiber, a slanted isotherm occurs across the fiber [Figure 8]. A grain nucleated on the cooler side of the fiber will have more time to grow than grains on the hotter side of the fiber, which must wait until it sinks down below the peritectic temperature. The grains on

the cooler side will be able to crowd out other grains. As the fiber continues to move and this grain exits the hot zone, the grain grows to keep up with the peritectic temperature isotherm as is regulated by the hot zone. In this situation, a considerable amount of growth must occur along the c-axis to keep up with the moving growth front, since the grain is misaligned with the axis. Growth in this direction is slower, and if it falls behind, a new grain can nucleate ahead of it and crowd it out. If this happens repeatedly, the slanted grain microstructure results. If the grains are polished along a cross-section which slices through the slanted grains at the wrong angle, the microstructure reveals short, blocky grains, instead of slanted grains. The particular cross-section examined often results in distorted projected angles for the grain orientations and grain boundaries, so one must take care before drawing too many conclusions about the angles of these features from a polished cross-section.

If there is inadequate mechanical control of the fiber in the furnace, the fiber may move closer to one side of the furnace, and a slanted thermal gradient can result. This can easily happen since the fiber hangs freely and can swing. Also, if the fiber is not perfectly straight, a slight bend can cause one section to be closer to one side when it passes through. The geometry of the furnace may create a non-uniform gradient if the heating element is not arranged perfectly symmetrical in the furnace. Extra care must be taken to avoid these problems.

An attempt to improve the azimuthal thermal uniformity was made by reducing the sideways motion of the fiber with tubes, having an inner diameter of 1/16", as guides around the top and bottom the fiber to keep it better centered. No noticeable improvement was obtained from this modification. The lack of success may simply be an indication of an asymmetry in the coil arrangement. Better efforts may be required to even out the thermal gradient.

The growth rate and temperature had little correlation with grain length, as can be seen from Table 1. This indicates that other factors are responsible for limiting the grain length. Under certain conditions with certain materials, too high a growth rate and too low a temperature gradient would lead to dendritic growth or equi-axed grains in extreme cases. However, these features did not appear in the melt-recrystallized YBCO. The instability of the growth front from segregated composition is not the limiting factor for YBCO grain length under the conditions used.

The majority of the microstructure after the initial melt zone is full of small inclusions, pores, and parallel stripes running between the platelets. What varies is the density of these features, the orientation of the parallel stripes, and the length of the grains. Also present under polarized light are twinning planes. The degree of twinning appears to vary within different samples which experienced the same oxygen annealing cycle, and it is not known why this might occur.

Stripes

Common in virtually all the samples were long parallel stripes oriented along the a-b planes. SEM examination of polished cross-sections reveal that the polish occurred across the platelets, and that the stripes result from the platelets tearing, probably during the grinding process. One possible explanation is that these parallel features are cracks resulting from stresses as the material passes through the tetragonal to orthorhombic phase transition. As single grains become larger by melt-recrystallization, the stresses are larger and may be enough to delaminate between platelets. The stripes are often ragged and appear too wide to be cracks. Grinding and polishing could tear at any cracks and make them appear to be wider then they really are. Also, the plane of the polishing cross-section often slices through these parallel planar cracks at an angle, causing the crack to appear wider. The samples were handpolished starting with 200 grit, then 600 grit SiC paper, followed by progressively finer diamond pastes. Some samples were buffed in a silica colloidal polishing media as a final step.

Another more plausible explanation is that a liquid phase gets trapped between the platelets as the platelets grow. If the crystal growth front consists of layers of platelets growing into the liquid, excess liquid may get entrapped between the platelets. A model for this is proposed by Goyal, et al [3]. The anisotropic growth rate in YBCO causes slender platelets to grow forward out into the liquid before thickening and merging together. When it encounters a 211 particle, some portions of the platelets get blocked, but the rest continues. The result is a trail of liquid behind the 211 particle. Eventually the platelets grow in thickness and squeeze out or consume some of this liquid, but the rest gets left behind. The microstructure then consists of many platelets separated occasionally by a layer of what was liquid phase. The liquid boundary between the platelets are flat and smooth and thin relative to the platelets, unlike the parallel stripes observed in this study.

This liquid phase could react during storage before testing. YBCO is known to react with moisture and CO_2 at room temperature to form $BaCO_3$ [22]. Subsequent polishing could then produce the stripes as the grinding removes the second phase. Another possibility is that the liquid phase etches away during grinding (which was done in water) and subsequent polishing. An alternative is that the entrapped liquid might react during grinding to form a harder material, which would get pulled out during grinding. The tearing would result in ragged edges found in the stripes.

The stripes are not observed in the slowly melt-processed samples examined in Goyal, et al [3], which were generally cooled at 1°C/hr. This may simply be due to better polishing methods. However, the faster growth in a thermal gradient used in zone melting may cause larger amounts of liquid to get entrapped between the particles. Faster growth would allow less time for the liquid to diffuse ahead of the growth front, and larger amounts would fall behind to be engulfed by the advancing platelets. These large sections of liquid could form wider features than the thin, narrow liquid phase

observed in slow melt-processed samples. This would suggest that a much slower growth speed in the zone-melting furnace would eliminate the stripes. However, using a growth speed as low as 1.6 mm/hr had no effect to reduce the presence of stripes.

If the liquid is a non-equilibrium phase caused by cooling too quickly, it may be possible to remove some of this liquid after entrapment by soaking the material at a high temperature just below the peritectic to allow the liquid to react with the 211 phase. This may be done by allowing the barium-cuprate-rich liquid time to react with 211 phase and form more 123 material. This technique could be done either by a separate anneal around perhaps 950 °C, or by creating a more shallow temperature drop at the exit of the zone melt furnace so that the freshly solidified material spends more time at high temperatures close to the peritectic before being cooled below the point at which liquid phase can still react to form more 123.

Another possible explanation is that the observed features are not pullouts, but are actually many pores flattened between the platelets. The pores could result from bubbles produced by CO_2 gas, which has been observed in YBCO above 900 °C [8]. Carbon segregation has been shown to occur in YBCO [10], so this might add to the favorability of CO_2 gas formation at the growth front. The gas could be oxygen evolved during the reduction of CuO to Cu_2O.

A brief discussion of pore formation with respect to metal solidification is given in Reed-Hill [6]. Bubbles already formed in the liquid can give elongated pores where directional solidification occurs. Dendritic growth can produce pores by another mechanism, where shrinkage upon solidification creates a vacuum between dendritic arms, and the arms thicken and close together making it difficult for a viscous liquid to penetrate. Gas bubbles may nucleate in this lower pressure at the root of the dendritic growth front.

The anisotropic growth of YBCO causes platelet growth to dominate the growth front. Bubbles which become entrapped would form flattened pores elongated in the growth direction. The flattened shape arises from an attempt to reduce surface energy by reducing its dimensions along the planes with higher surface energy, i.e. the 100 planes [7].

Pores are observed in the quenched melt zone, lending plausibility to the pore theory. The main flaw with this idea, however, is that some sections also contain round pores in the same region with stripes. If the stripes are deformed pores, it is hard to explain their coexistence with round pores. It may be that the flattened pores result from bubbles of a critical size, which forms the flattened pores, while the other pores are able to remain round because their size causes them to remain stable spheres within the advancing growth front.

Whether the features are due to gaseous phase or to liquid phase entrapment, their likely segregation at the growth front may explain some of the difficulty in growing long single grains. Segregation of a second phase at the growth front hinders the advance of the growth front by acting as a barrier to components needed to form more 123 at the front. If the growth front is impeded too much, a new grain may nucleate ahead of the growth front. The longest grains were usually obtained in the initial melt-zone, which was free of stripes. The long grains that did manage to persist over an extended distance in the region beyond the initial melt zone almost always consisted of long parallel stripes oriented along the axis [Figure 9]. This could indicate a stable condition where the gas or liquid phase gets entrapped and removed from the solidification front, reducing accumulation so it never seriously impedes the growth front. However, though phase segregation impediment may occur, evidence exists that it is the non-uniform azimuthal temperature gradient that is the most crucial factor in growing long grains [27].

Other Features

At the growth front, pores or pullout have been observed in quenched fibers [Figure 10]. The growth front in this case contains stripes. This lends credence to the idea of a segregated phase at the growth front which gets incorporated between platelets to form stripes.

SEM micrographs of fractured surfaces reveal platelets. These are shown in Figure 11. This type of structure is typical in melt-processed YBCO, where the growth anisotropy results in platelets. In one sample, there appears to be a small gap between platelets [Figure 12]. This gap could be evidence of the feature which forms the stripes. It could be the result of the removal of a liquid phase material which got pulled out when the specimen was fractured, or this feature may be evidence of the flattened pore described above. The boundaries of this gap are smooth faces of the platelets. This feature could result in a ragged stripe if grinding and polishing tore at the boundaries.

Examination of the surface revealed a coating of needle-like 211 particles and a liquid-like phase on the fiber [Figure 13]. It does not have markings suggesting the layered platelet structure which it covers. This coating probably results from the peritectic melt in the melt zone dripping down and covering the surface of the melt-recrystallized fiber below it. The peritectic melt drip would be quenched before it could react and form the equilibrium 123 phase. It is not known what effect this coating has on the electrical testing. An attempt to remove this was made by roll milling a fiber 36 hours in a ¼" inner diameter alumina tube with 15 μm diamond powder and alumina beads as grinding media. Examination by SEM revealed that the coating appeared to be removed [Figure 14]. This process decreased the surface resistance by 40%-60% [Table 2].

An alternative approach to coating removal assumes the coating is a quenched peritectic melt in a non-equilibrium state, and that it can be reduced or eliminated simply by annealing at a high enough temperature for the 211 and liquid to react and form 123 phase. An experiment to validate this approach was done by heating a melt-textured fiber to 960 °C for 2 hours in air. SEM examination revealed that the original coating was annealed out by the heat treatment, though it was not clear if it was completely removed, and if the surface was completely 123 phase.

The initial melt zone is usually the best quality, having the longest grain. It never has stripes. One possible reason for this is that the amount of second phase segregation at the advancing growth front is initially too little to produce the stripes. The second phase might need a certain distance to accumulate before it can produce observable stripes. Another reason for the lack of stripes may be that if the liquid phase is Ba-Cu rich, it will be more likely to react in the initial melt zone. This is because there is a large excess of 211, which readily consumes Ba and Cu compounds to form the 123 phase. Similar behavior has been observed in melt-textured YBCO produced after wicking away liquid in the peritectic melt [19]. This study showed the material to have grain boundaries free of any liquid phase. If the stripes observed in zone-melted fibers are liquid phase, the wicking would reduce or eliminate the liquid phase between platelets.

The longer grain length found in this section may be due to a lack of a segregated second phase at the advancing growth front. This would support the idea that the segregated phase at the growth front acts to impede the advancing growth front, allowing new grains to nucleate ahead of the growth front.

Whatever the cause of the improved microstructure in the initial melt zone, the phenomena might be exploited by increasing the 211 content in the material over the whole length to produce the improved microstructure. This could be done by increasing the initial 211 composition. It could also be done by wicking away the liquid by placing the melt in contact with porous 211, which would act as a sponge for the liquid [19].

Unfortunately, it is not even known if this microstructure is desired. Since it only persists over ~ 1 cm, it is too short to perform radio frequency tests with the available equipment. It may be that the high ratio of 211 results in an undesirable percolation path during AC conduction. This structure may have fewer of the pinning sites required to prevent power loss. The lower fraction of superconductor may increase the surface resistance, and may outweigh the benefits of fewer grain boundaries. On the other hand, grain boundaries in this type of structure with a misorientation up to 27° are still found to have high Jc values, presumably due to cleaner grain boundaries [19].

B. Electrical Testing

As was stated earlier, it was found that silver lead attachment only served to decrease the measured Q's. For example, the Q at 20 dBm went from 4400 to 5905 by removing the silver contacts. As a result, all testing was performed without silver lead attachments. Two possible factors could be responsible for the lower Q. Poor contact resistance between the silver and the YBCO could hinder the effectiveness of the leads. More importantly, the silver painted on the surface would conduct the current over that section of fiber, so the additional losses will be associated with the resistance in the silver.

A typical plot of the reflected power versus frequency is shown [Figure 15]. The width of this peak is used to determine the Q. The Q must be corrected, since it is affected by losses in the external cables and connections to the cavities. The Q resulting from the cavity and cables, called the loaded Q, is measured from the reflected power peak at resonance, and is equal to

$$Q_L = \omega_o / 2\delta\omega$$

where ω_o is the resonant frequency and $\delta\omega$ is the width of the peak at half the power. The Q that results from the conductor is the unloaded Q, Q_U. The following relation [25]:

$$1/Q_L = 1/Q_U + 1/Q_E + 1/Q_{E'}$$

relates the loaded Q with the unloaded Q and the Q's resulting from power losses in the line leading to the cavity (Q_E), and power losses along the line leading back from the cavity ($Q_{E'}$). This equation assumes the losses in the cavity walls are negligible, which is true for most of the samples measured. The Q_E and $Q_{E'}$ are minimized by increasing the spacing between the electrodes and the YBCO conductor, which reduces the coupling, so fewer losses exist in the external lines. These losses can not be completely eliminated, otherwise the signal becomes too small. The Q_L must still be corrected to obtain Q_U. This is described in the Appendix.

The Q is used to calculate the surface resistance (R_S). The insertion loss is measured and used to calculate the magnetic field power (H_{rf}) at the surface of the conductor. The method of calculation is shown in the Appendix. The surface resistance at -10 dBm is listed as a representative value for the surface resistance of each sample in Table 2. There was no apparent correlation between processing conditions and the surface resistance, indicating that hidden process variables such as the azimuthal thermal gradient are probably more responsible for the surface resistance.

The rf testing revealed an increasing surface resistance for increasing power levels. The R_s dependence on magnetic field power is expected to be linear where

grain-boundary Josephson junctions are the main cause of power loss, and should vary with the square of power if the intrinsic resistance dominates power losses. The implication is that good quality samples with few grain boundaries will have a lower R_s, but they will rise faster with power.

The surface resistances for this study generally fit the linear equation:

$$R_s = R_{so}(1+\beta H_{rf})$$

which corresponds to weak-link dominated losses. The R_s dependence on magnetic field power is shown for a typical sample with low surface resistance and one with higher resistance [Figure 16 and 17]. The remaining samples for which the power dependence was measured are shown in the Appendix.

The R_{so} ranged from 9.4×10^{-5} to 6.1×10^{-3}. The fitting constant β ranged from 0.002 to 0.1. A small negative quadratic term also appeared in some samples, indicating that the surface resistance was tapering off with increased power, and that the sample was probably approaching saturation with applied field. This quadratic term was largest for the samples with high surface resistances, so one might conclude that the poorer samples were closer to saturation. The R_{so} and fitting constants are listed in Table 4.

The surface resistance of a few fibers was measured at higher harmonic frequencies. The resistance was found to increase with frequency, as can be seen in Figure 18. The nature of the frequency dependence can not be shown, however, due to the limited frequencies able to be tested.

An examination of some selected fibers revealed a rough correlation between the microstructural features and electrical performance. The microstructure of the samples with low surface resistances have long grains well aligned with the fiber. There were often stripes running parallel with the fiber, so stripes are deemed relatively harmless to the electrical performance. The microstructure of the samples with higher surface resistances have shorter blocky grains which tend to be more misoriented. Even though the current conduction is only affected by the surface microstructure, the interior of the polished cross-section appears to correlate with the electrical results, suggesting that the quality of the interior of the fiber is representative of the thin layer at the surface over which the conduction takes place. In other words, grain boundaries extend out to the surface, and are not superceded by conduction through any thin continuous coating which may exist on the surface.

The average grain lengths for these samples are listed, along with their respective surface resistances [Table 3]. The surface resistance appears to decrease with increasing grain lengths, though there is a large degree of scattering [Figure 19]. Results reported in Hein, et al [30], which used samples with much smaller grain sizes,

show a linear relationship between (grain size)$^{-1}$ and surface resistance. If weak links at grain boundaries are shown to provide an easy path for flux motion, then short grains, even though each may be fairly well aligned, would result in power losses because of the higher amount of grain boundaries. The data in this thesis has a definite increase with increasing grain length, but the high degree of scattering indicates that other factors heavily influence the surface resistance. For example, one particular sample, which had short grains but a low resistance, also had few stripes or any other inclusions, and appeared to have clean grain boundaries.

The amount of twinning observed tended to be highest in samples with low surface resistance, though this was not always the case. Twinning defects contribute to a low surface resistance by adding more flux pinning, but it may be more significant that they represent material in the orthorhombic phase. Heavily twinned material would be well oxygenated, and would have more superconducting electrons available, resulting in a lower surface resistance.

It is not clear what role the stripes may have in the electrical performance. The stripes are likely to be non-superconducting, may be thick enough to form a barrier to conduction. However, the barriers are discontinuous, current can often be bypass the barriers through gaps, according to a brickwall model. The stripes could aid conduction if the material surrounding the stripes is made richer in pinning sites, as occurs around 211 particles [18]. The best samples had extensive stripes, so they probably are not significantly detrimental to the surface resistance of the fibers.

The alignment of the grains is also expected to affect the surface resistance. Misoriented grains require that some conduction occur along the c-axis. The conduction along this axis is weaker, so power losses may result from this. Also, misoriented grains present a greater number of platelet boundaries that current must cross.

It is not known how these microstructural features may affect the surface resistance, since it is hard to quantify some of these features, such as twinning and grain misalignment. Another complication is that often the features only exist in certain sections of the material, and so a method of weighting the various effects according to the amount of the various features and their location must also be devised. The location of the defect in the fiber is important, since the resonating wave results in more current at the middle of the fiber than at the ends. In addition, it is not yet clear how much of these features are produced during polishing. Reaction with water and rough grinding may thicken stripes and may cause the material to appear to have more stripes than they actually do. Similar arguments can be made for the inclusions. Issues with sample preparation and quantification of microstructural features make it difficult to carefully relate surface resistance to microstructure. However, the average grain size appears to correlate with the surface resistance.

V. Summary

The melt-recrystallization process results in longer grained samples, with the axis of best conduction along the fiber's long axis. Possible causes of the stripe features observed in the microstructure are discussed. The likely cause is suspected to be from liquid phase entrapment. The range of different growth temperatures and growth speeds used were not found to significantly affect the microstructure. The grain length may be limited either by phase segregation at the growth front, or by azimuthal thermal gradients in the furnace.

Melt-recrystallization by a zone melting furnace improves the materials properties to achieve lower surface resistance. The measured surface resistances, which ranged from $1x10^{-4}$ to $6x10^{-3}$ Ω, are equal or greater than those of poly crystalline samples measured in other studies. However, it is suspected that the powers used in this study are higher than that used in the numbers cited, so a more relevant value for comparison is $2x10^{-1}$ Ω, which was measured on a polycrystalline sample at saturation fields [33]. The saturation field of thin films is higher than for polycrystalline samples, so its surface resistance will still be $\sim 10^{-5}$ at the powers measured. The surface resistance of the zone melted fibers was better than polycrystalline samples of other studies, but still a factor of 100 higher than that of thin films.

Samples with longer grains tend to have lower surface resistances. The R_s had a linear dependence on magnetic field power, suggesting that the behavior is still very much weak-link dominated. Improvements may be achieved with better control of the melt-recrystallization process to achieve longer grains. A surface coating was observed on the fibers, which served to increase the surface resistance. This coating may be responsible for the linear R_s dependence and the high R_s. The slight negative deviation from the linear behavior seems to indicate the onset of saturation at high fields, another indicator of poor material quality.

The best surface resistances measured were two orders of magnitude higher than that of thin film stripline samples, but the YBCO fibers still had lower surface resistances than copper, making them valid replacements for copper. Greater improvements would be expected near liquid helium temperatures.

IV. Future Work

Further investigation could be done to improve the zone melting furnaces. Better methods to even out the azimuthal thermal gradient should be explored in an

attempt to increase the grain length. These techniques could focus on better centering of the fiber in the hot zone at the solidification front.

Another direction for further work is to verify the importance of the surface coating and to investigate methods of removal. Once a technique for complete removal has been found, it should be determined if the surface resistance behavior is the same as that found in this study, and to see if the surface resistance is indeed near the power saturation level.

The effect of silver contact leads should be examined when they are applied to fibers in which the coating has been removed. It may be that the silver lead losses found in this study are due to poor contact resistance between the silver and superconductor due to an intervening surface coating. Attachment of silver leads will be of value when applying higher signal powers to the fiber, since the capacitive coupling method limits the maximum appliable power.

Lower surface resistances in improved fibers may require a new resonance test cavity, since the current copper cavity may be too lossy to accurately measure the fibers. A cavity constructed of superconducting materials might be designed and used to test fibers with very low surface resistances.

VII. Tables and Figures

Table 1

Growth Conditions For Melt-Recrystallization
All samples processed in furnace #4

Sample #	Growth rate	Set Point Temperature	Avg grain length (mm)
F4915	3.3 mm/hr	1000	0.56
F4111.1	3.3 mm/hr	1010	0.29
F4927	3.3 mm/hr	1020	0.71
F4119	3.3 mm/hr	1030	0.69
F4101	3.3 mm/hr	1040	1.04
F4104.1	-3.3 mm/hr	1000	0.67
F41011	-3.3 mm/hr	1010	1.34
F41012	-3.3 mm/hr	1020	0.43
F41013	-3.3 mm/hr	1030	0.80
F41015	-3.3 mm/hr	1040	1.86
F41029	9.9 mm/hr	1000	0.32
F4111	9.9 mm/hr	1030	Textured
F41024	5.0 mm/hr	1000	0.52
F41027	5.0 mm/hr	1030	0.59
F41018	1.6 mm/hr	1000	0.86
F41020	1.6 mm/hr	1030	0.56

* Negative growth rate values indicate drawing fiber in the upward direction

Table 2

List of measured samples and processing conditions

Sample #	Rs @ -10 dBm	Furnace #	Set Temperature	Growth rate (mm/h)
F185	4.06E-04	1	1020	3.3
F189	4.91E-04	1	1030	3.3
F192	4.95E-04	1	1000	3.3
F269	2.60E-04	2	1020	3.3
F2721	2.35E-04	2	1010	5.0
F2728	1.10E-04	2	1015	5.0
F292	5.59E-04	2	1020	9.9
F3279	1.26E-03	3	1025	-3.3
F3721	1.51E-03	3	1020	-3.3
F3726	6.80E-04	3	1020	5.0
F389	5.78E-04	3	1030	-3.3
F4611	1.03E-03	4	1015	3.3
F4618	1.88E-04	4	1015	3.3
F4630	6.53E-04	4	1020	3.3
F4719	2.57E-03	4	1020	3.3
F4726	2.90E-04	4	1020	5.0
F4816	7.42E-04	4	1030	3.3
F4820	2.60E-03	4	1020	-3.3

Table 3

Average Grain Length
(Sorted by grain length)

Sample #	Average length (mm)	Rs at -10 dBm
F4816	0.30	7.42E-05
F4719	0.60	2.57E-04
F389	0.67	5.78E-05
F4820	0.71	2.60E-04
F192	0.73	4.95E-05
F189	0.74	4.91E-05
F3726	0.78	6.80E-05
F292	0.82	5.59E-05
F3721	0.97	1.51E-04
F185	1.04	4.06E-05
F2728	1.26	1.10E-05
F2721	1.29	2.35E-05
F385, before polish		5.97E-05
F385, after polish		2.42E-05

Table 4

Coefficients of Rs dependence on Hrf

Rs=Rso(1+b1Hrf+b2Hrf^2)

Sample #	Rso	b1 (linear)	2 (quadratic)
F269	2.22E-04	1.09E-01	-1.62E-03
F2721	2.29E-04	2.72E-02	-1.51E-04
F2728	9.43E-05	7.51E-02	-5.29E-04
F3721	1.50E-03	2.66E-02	-2.79E-03
F3726	6.61E-04	4.81E-02	-1.10E-03
F3729	1.26E-03	4.76E-02	-2.40E-03
F4611	1.01E-03	6.01E-02	-2.59E-03
F4618	1.68E-04	9.06E-02	-9.82E-04
F4719	2.56E-03	2.73E-02	-3.11E-03
F4719 (2nd harmonic)	6.07E-03	2.90E-02	-5.98E-03
F4719 (3rd harmonic)	5.18E-03	2.27E-03	6.53E-04
F4726	2.77E-04	4.65E-02	-5.41E-04
F4726 (2nd harmonic)	1.11E-03	1.23E-02	7.84E-05
FE12-15	1.62E-04	3.48E-02	-5.24E-05
FE12-15 (2nd harmonic)	1.94E-04	3.30E-02	-4.87E-04

Figure 1

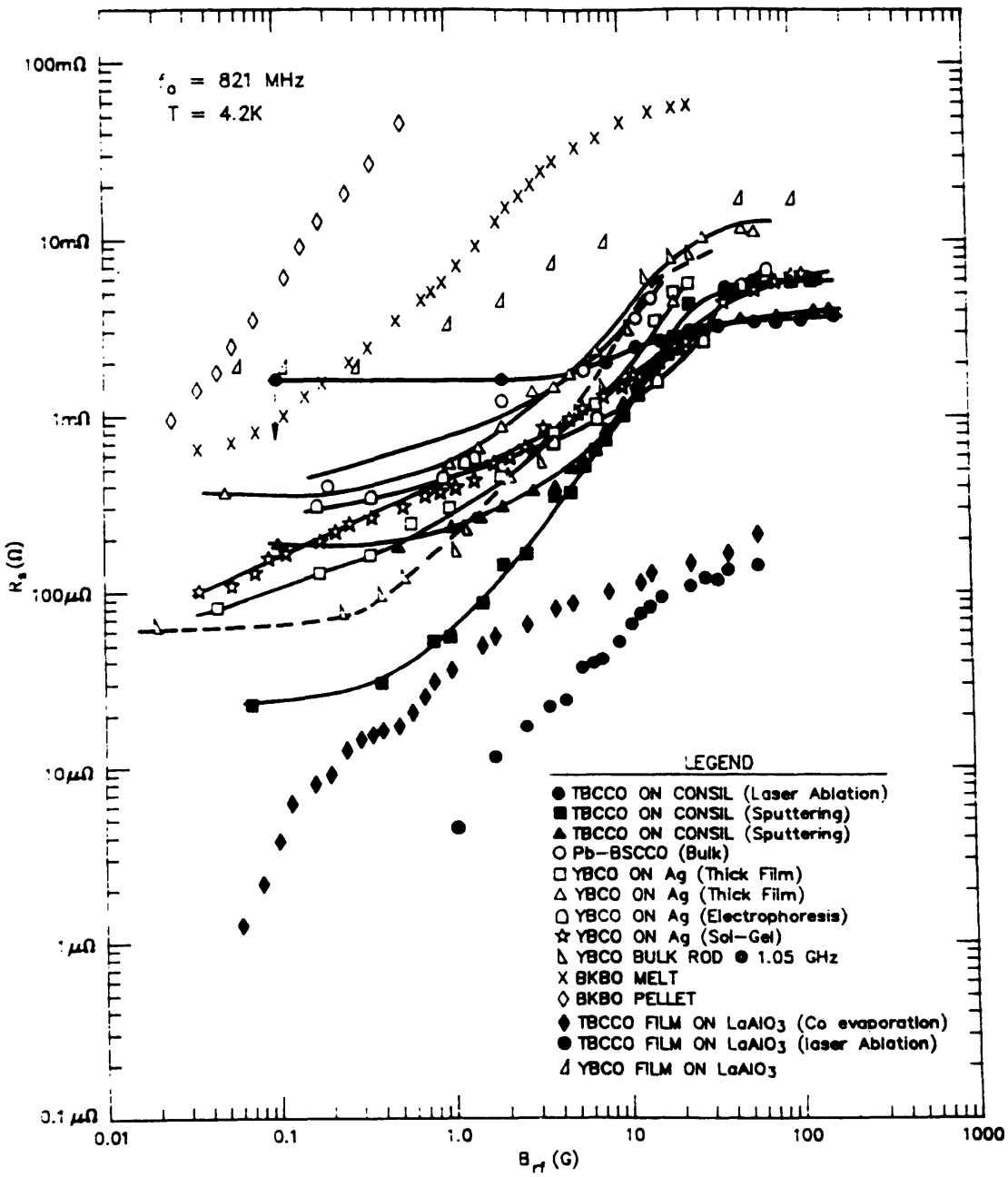

Fig. 1. Surface resistance vs. rf magnetic field at 821 MHz and 4.2 K for a variety of samples ([9] and J. R. Delayen, private communication). The behavior of a ceramic rod [1,2] is shown for comparison. The high apparent surface resistance of laser-ablated TBCCO on Consil is probably from the edges, which were not coated. Sample sources are given in the reference.

From reference 24

Figure 2

Zone melting furnace

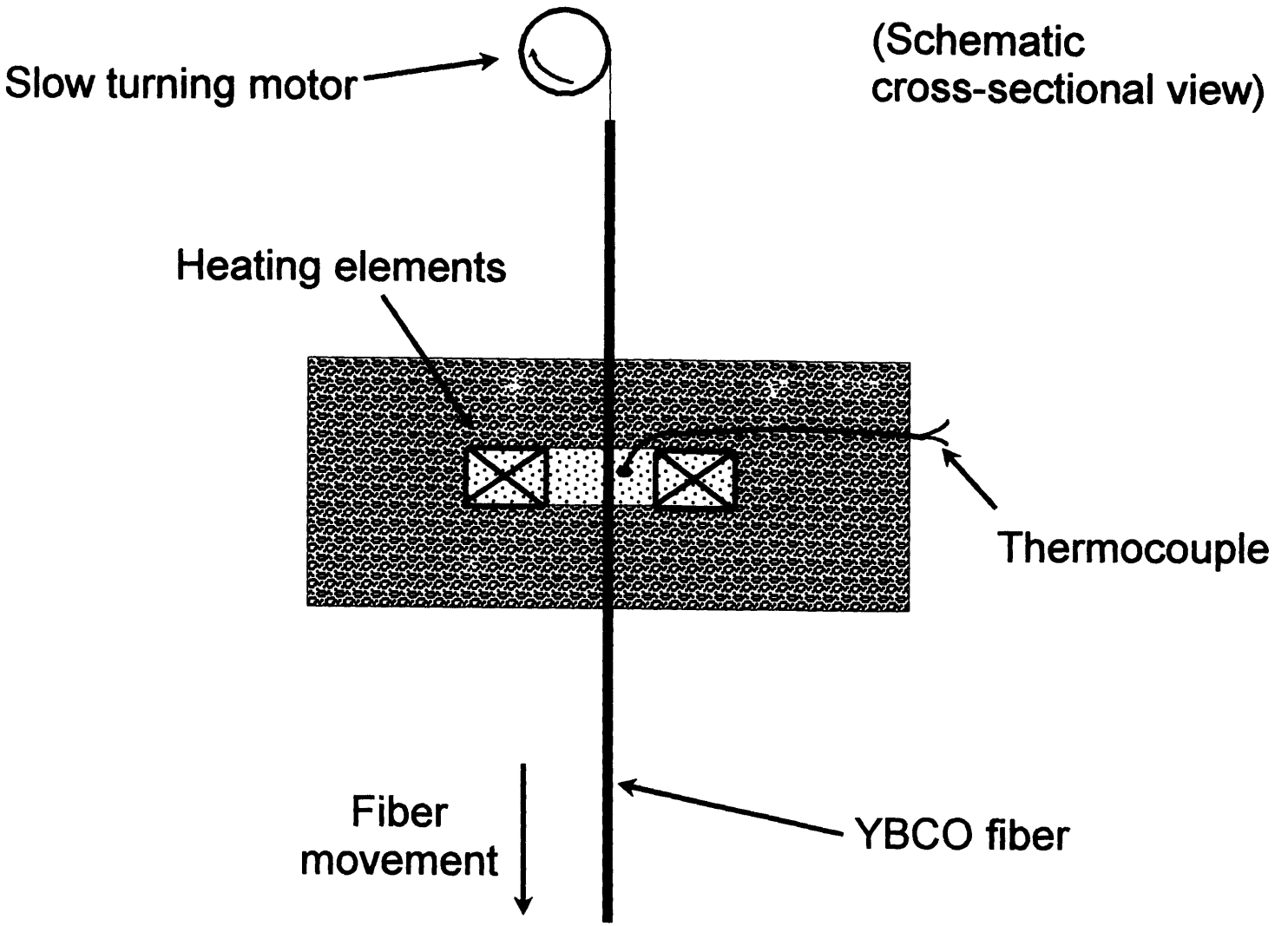

Figure 3

Copper Resonance Cavity

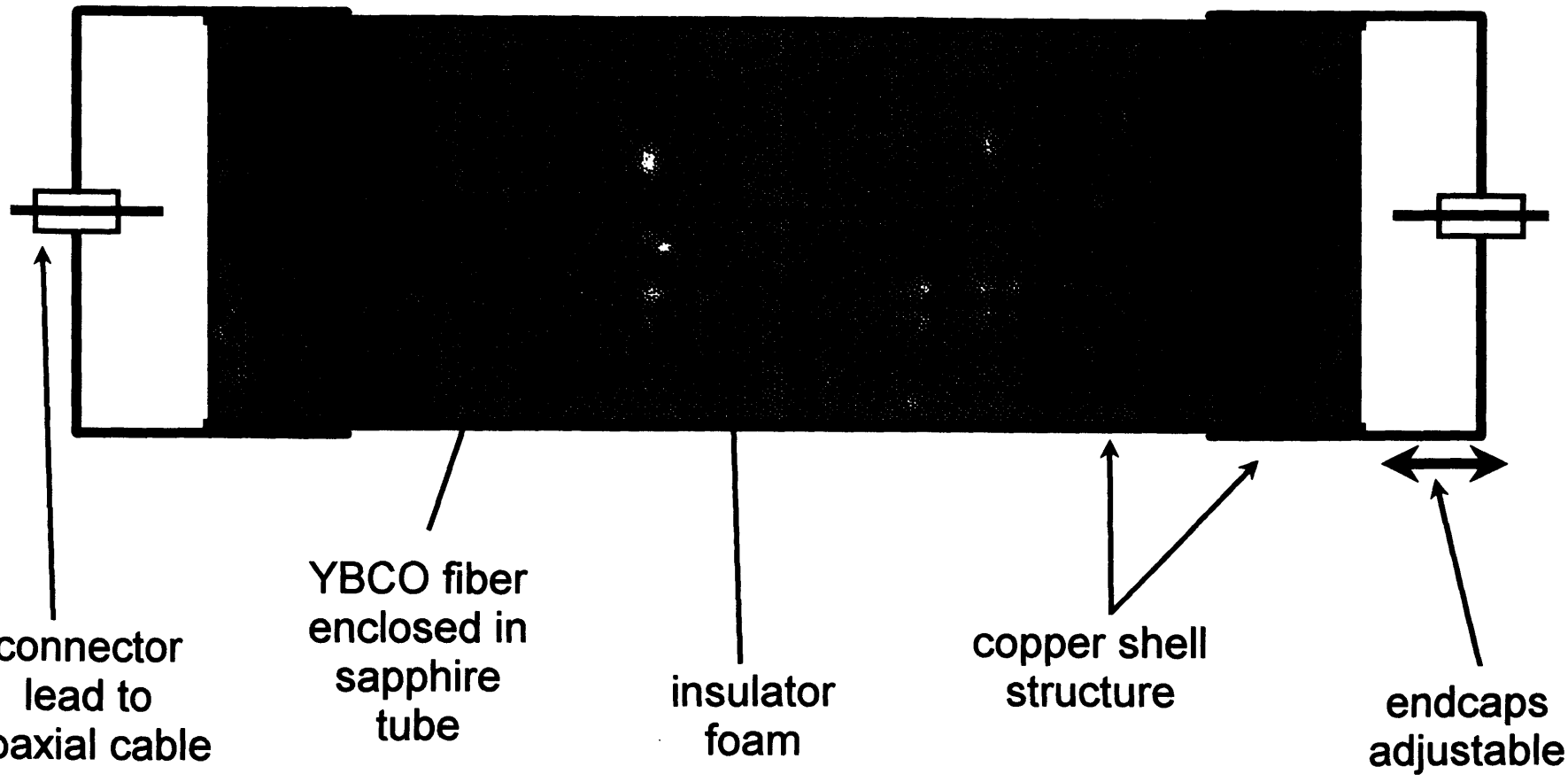

Temperature Profile Furnace #1

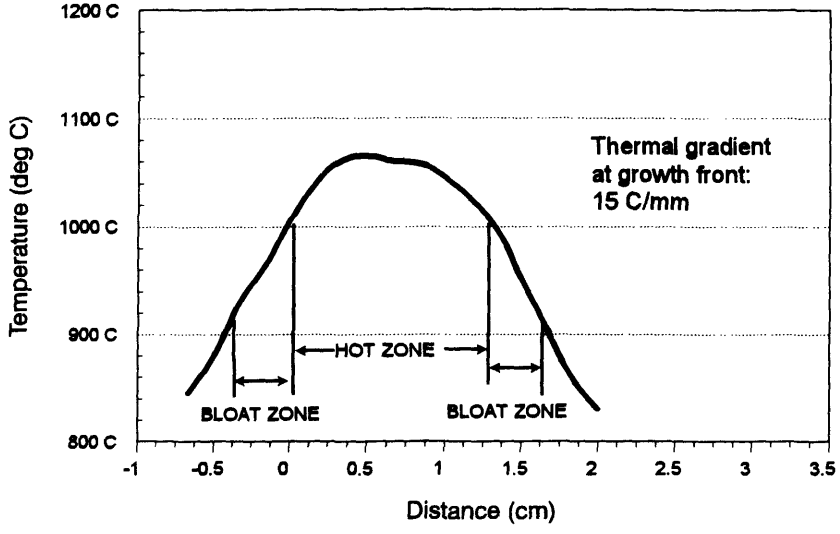

Temperature Profile Furnace #3

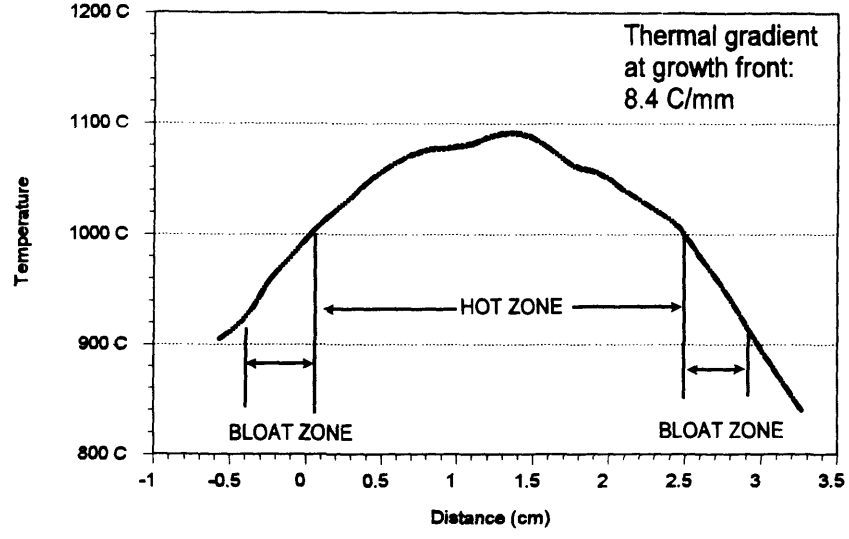

Temperature Profile Furnace #2

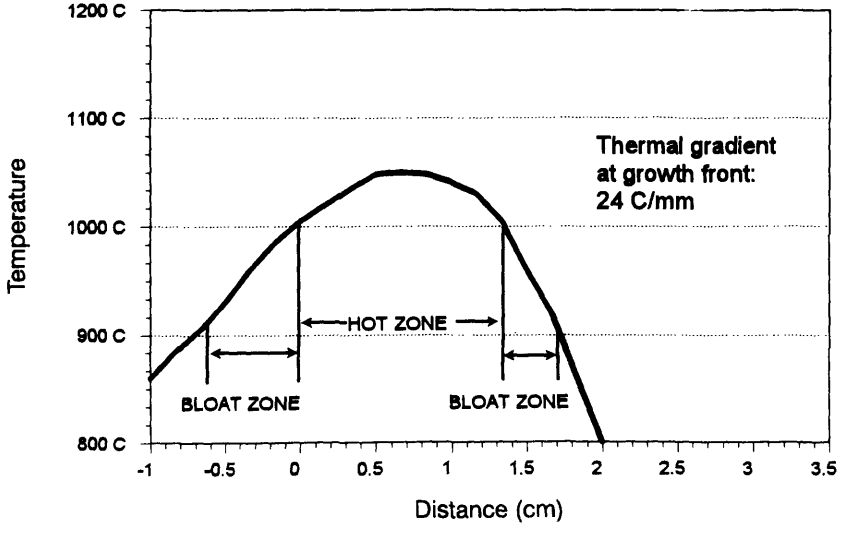

Temperature Profile Furnace #4

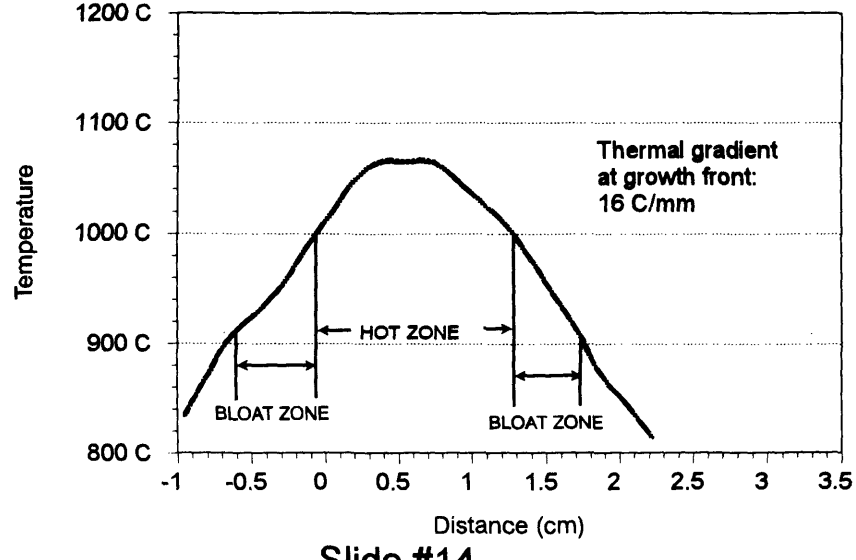

Slide #14

Figure 5

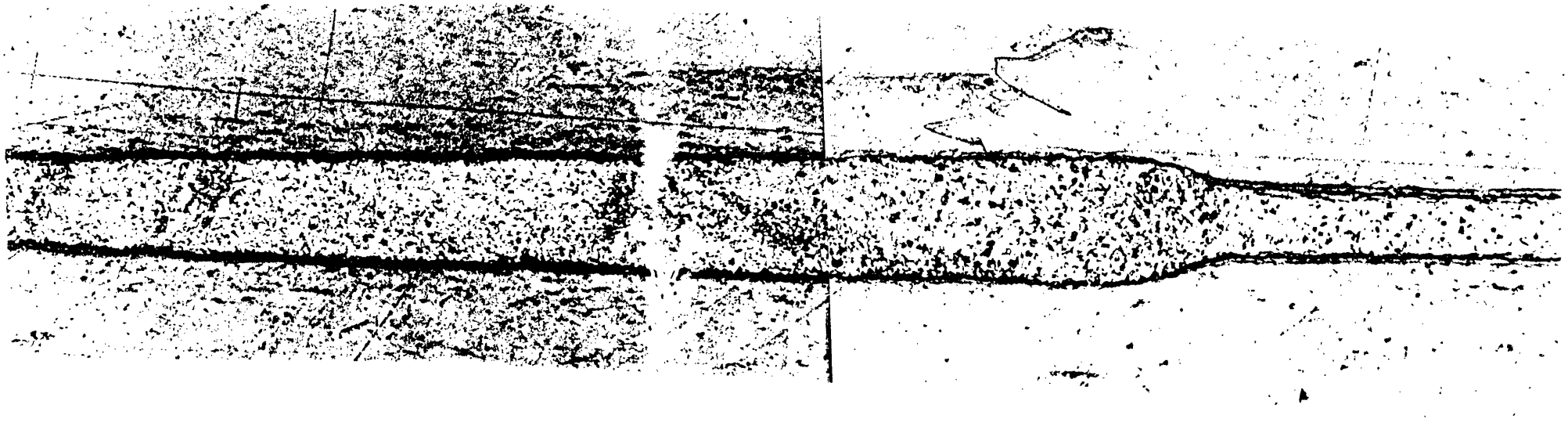

Typical bloat zone in a melt-recrystallized sample (40x).

Figure 6

Bell-shaped bloat zone in a melt-recrystallized sample (20x).

Figure 7

Slanted grain structure (80x).

Figure 8

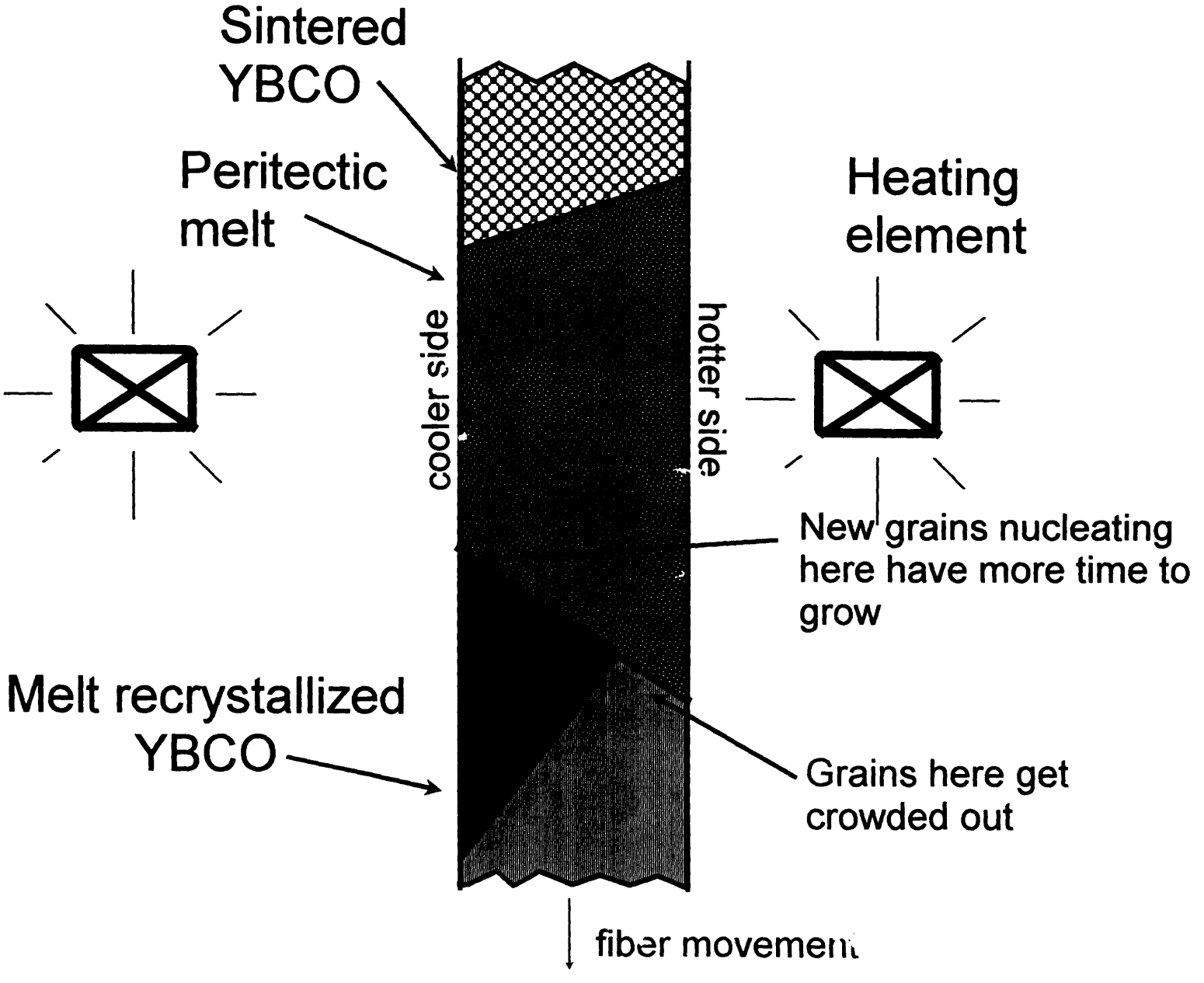
Sintered YBCO
Peritectic melt
Heating element
cooler side
hotter side
New grains nucleating here have more time to grow
Melt recrystallized YBCO
Grains here get crowded out
fiber movement

Figure 9

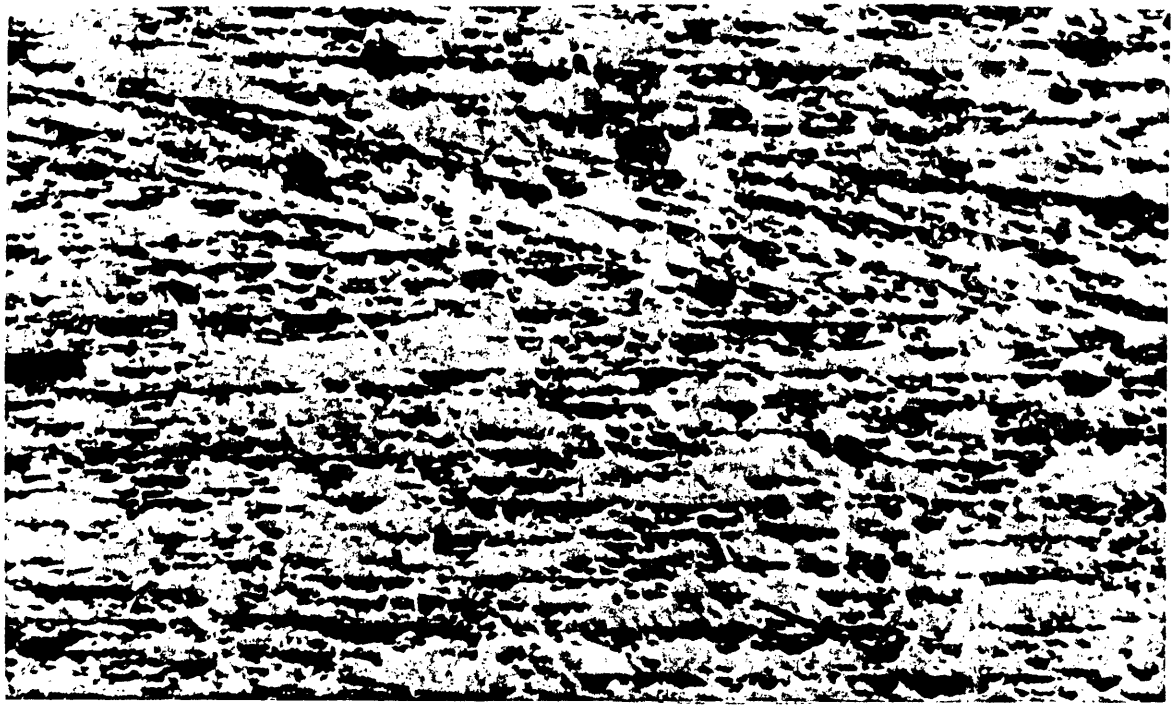

Striped microstructure (200x).

Figure 10

Stripes at quench front.(200x)

Figure 11

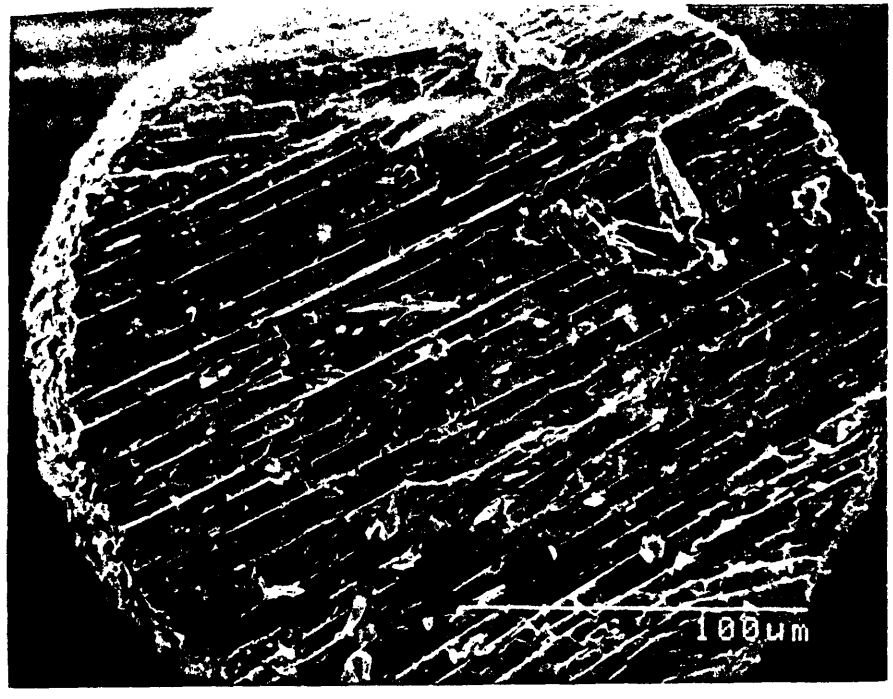

SEM photo of platelet microstructure (500x).

Figure 12

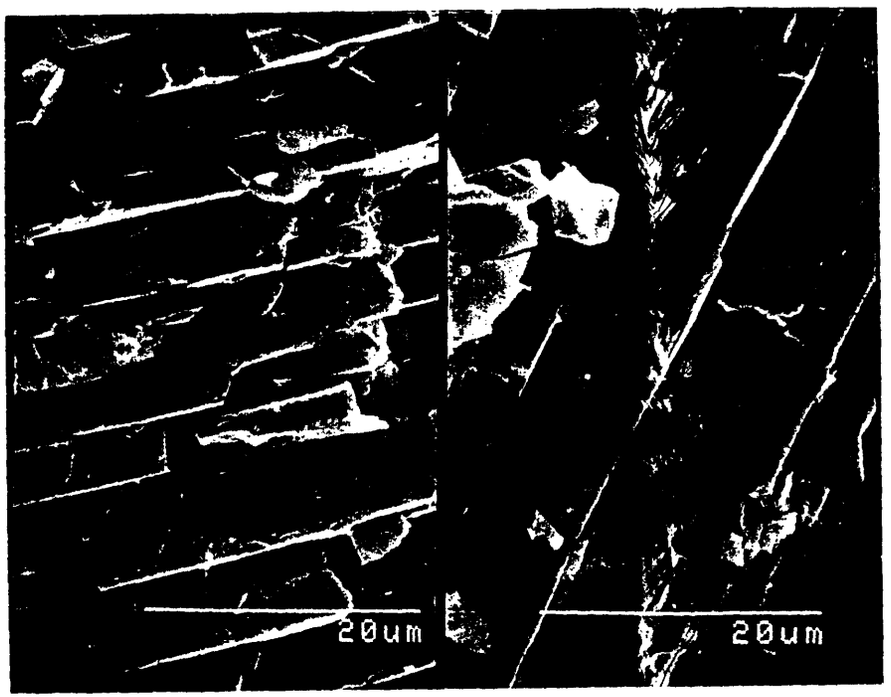

SEM photo of gap between platelets (200x).

Figure 13

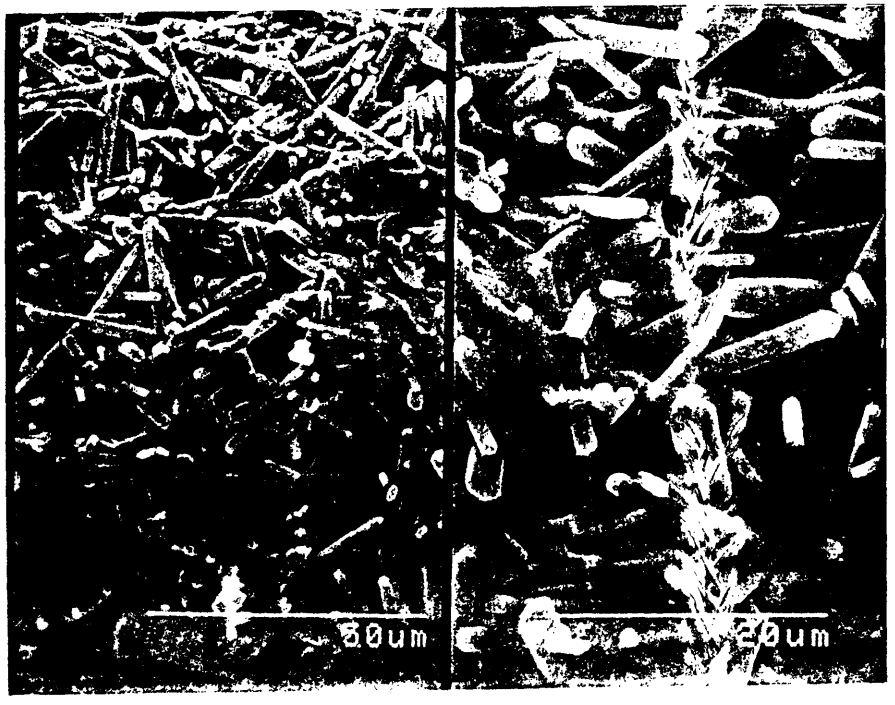

Surface coating on melt-recrystallized sample (800x and 2000x).

Figure 14

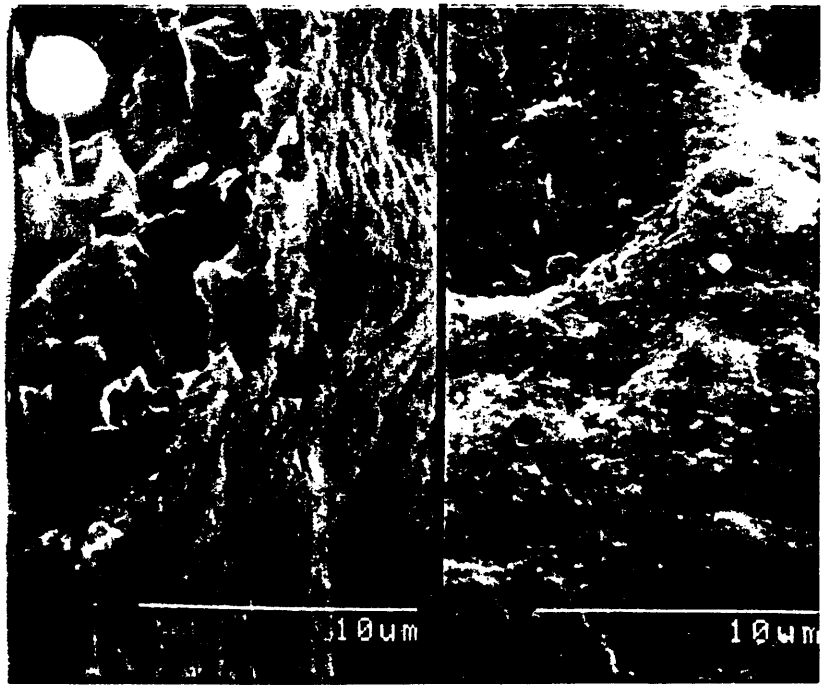

Surface after diamond powder polish (4000x).

Figure 15

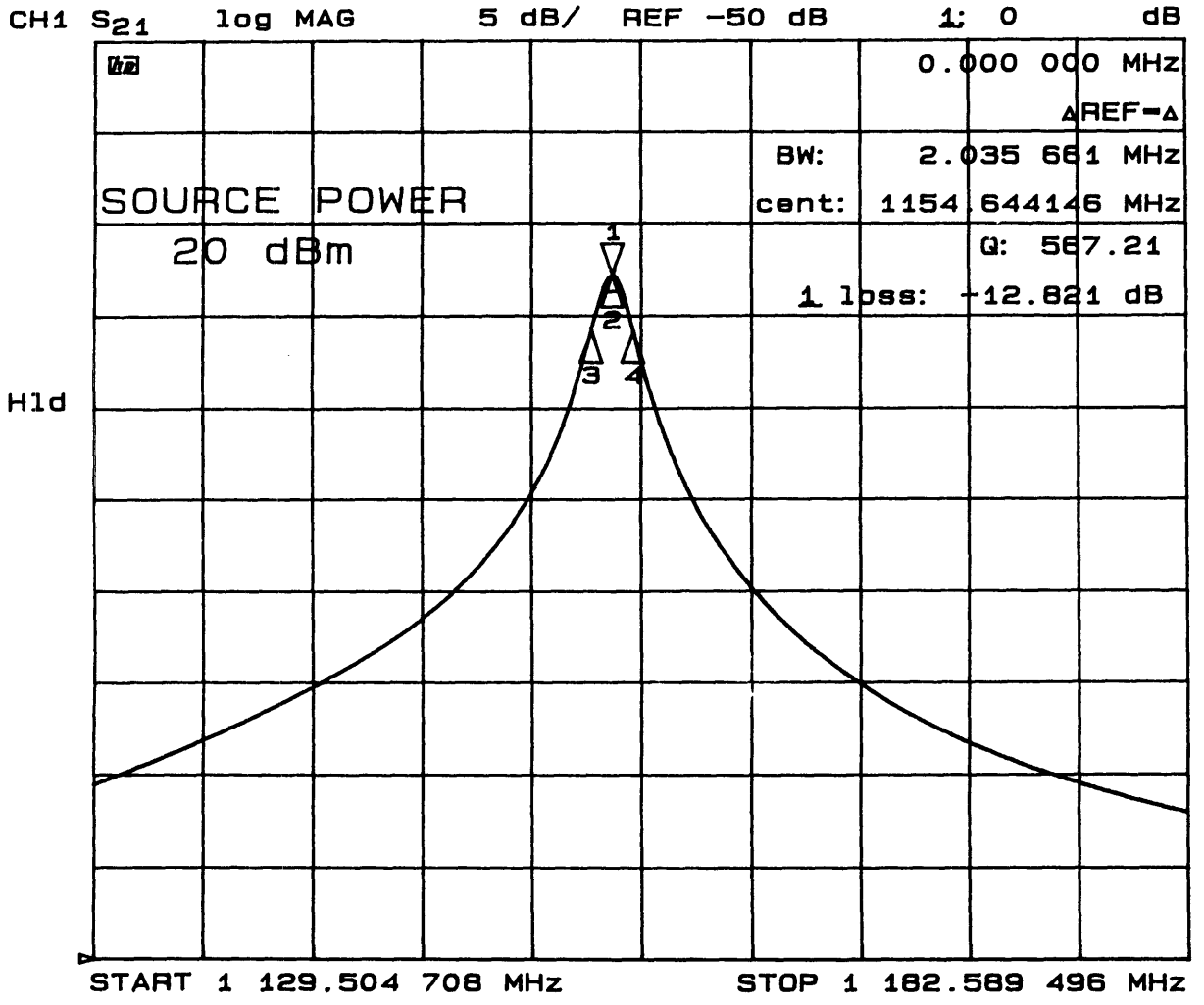

Typical resonance curve, from which Q is calculated.

Figure 16

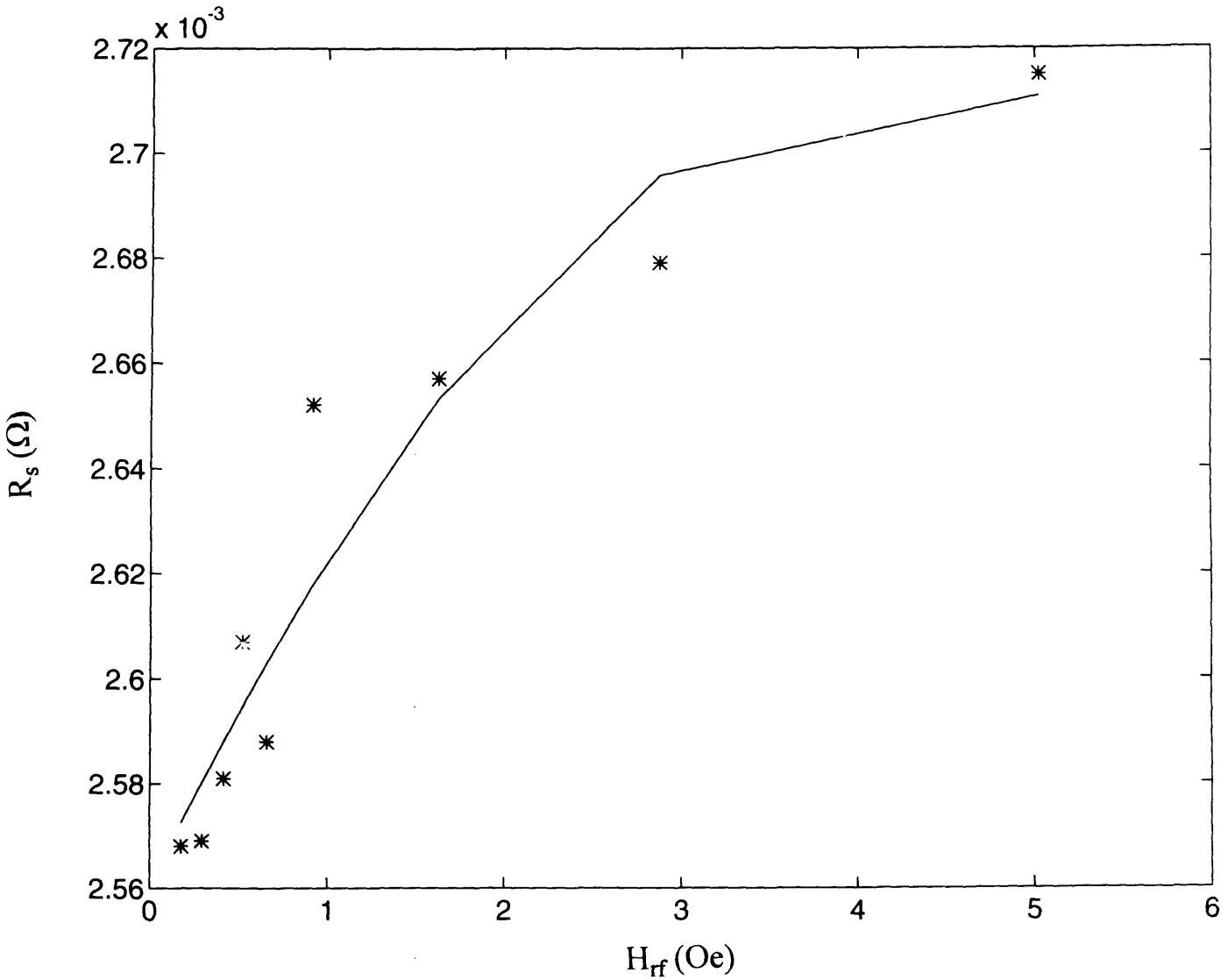

Rs plot vs Hrf curve of a typical sample with a high surface resistance (sample #F4719).

Figure 17

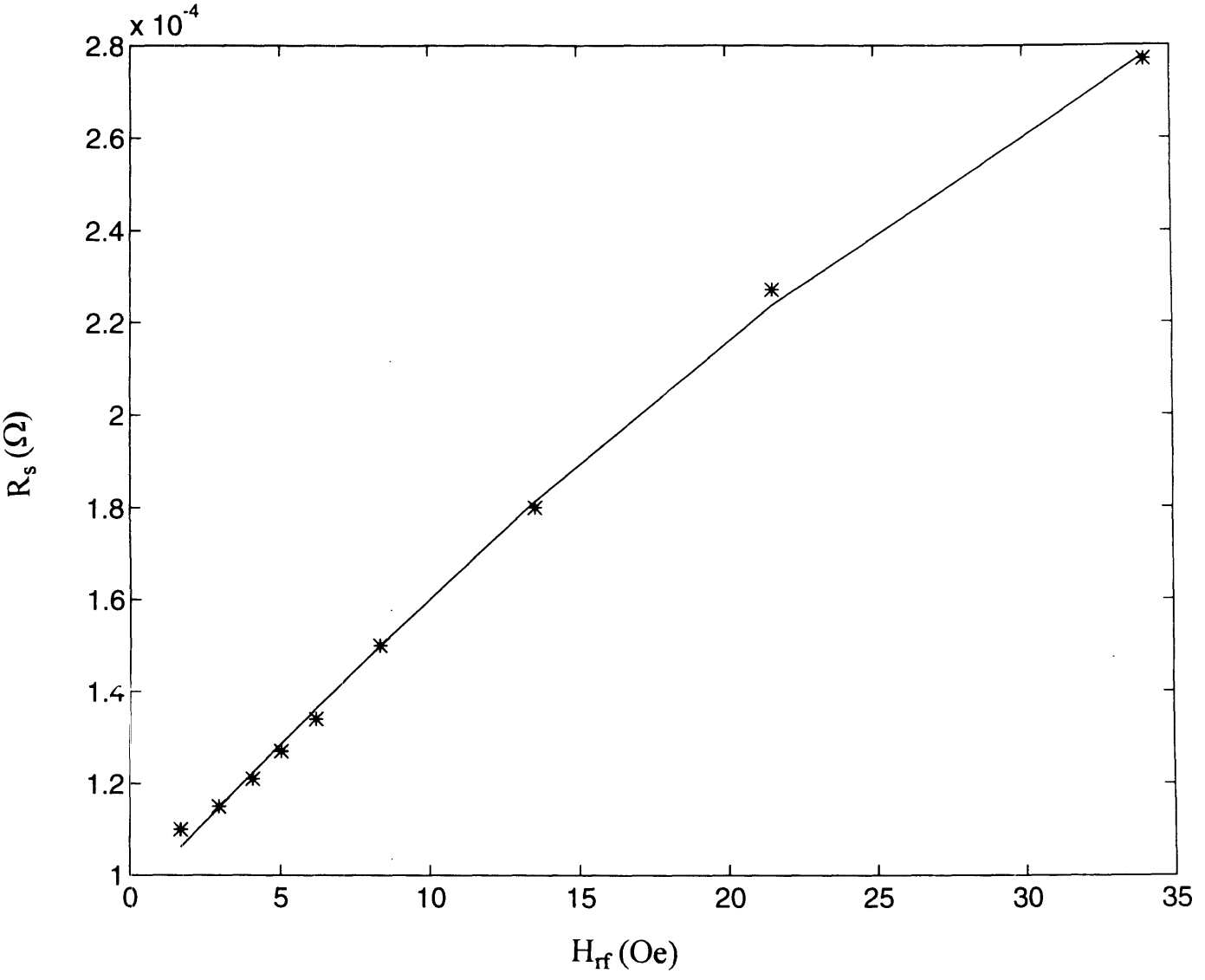

R_s plot vs H_{rf} curve of a typical sample with a high surface resistance (sample #F2728).

Figure 18

Frequency dependence of surface resistance

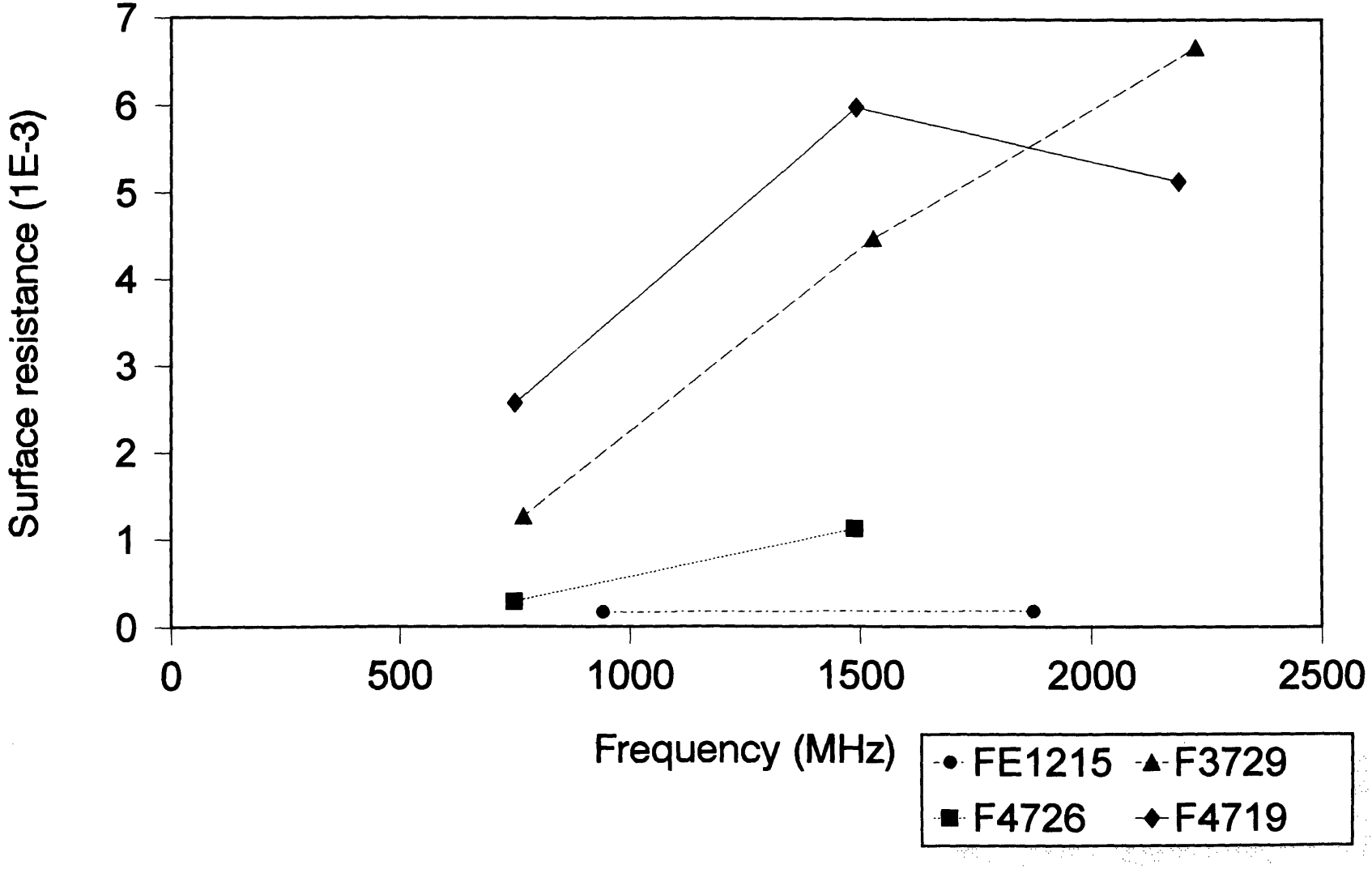

Figure 19

Surface resistance dependence on grain length

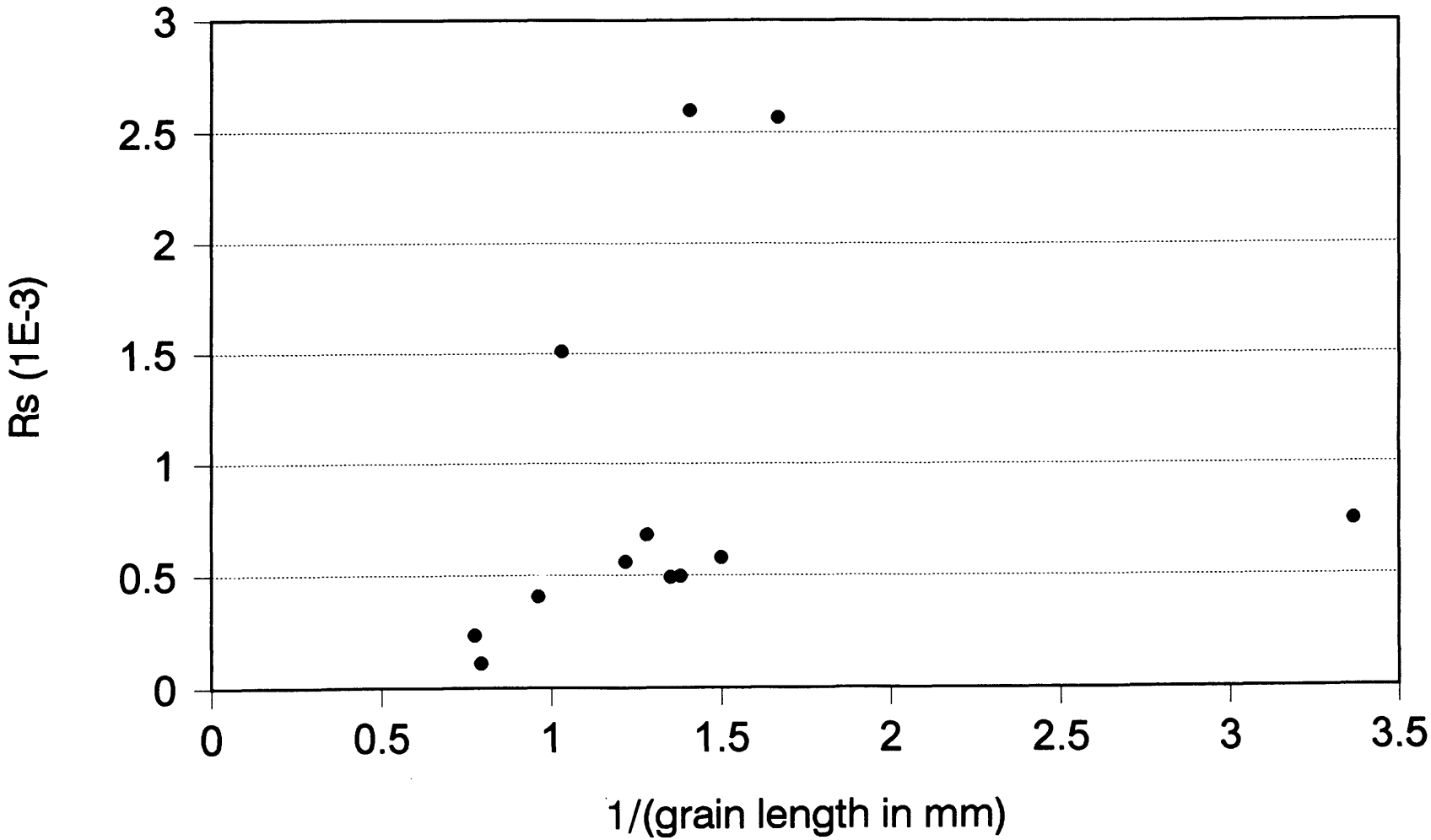

VIII. Appendix

A. Calculations

The measured Q is corrected for insertion losses in the following manner. Recall:

$$1/Q_L = 1/Q_U + 1/Q_E + 1/Q_{E'}$$

From [ref 25]:

$$T = \frac{4/Q_E Q_{E'}}{1/Q_L^2 + \left(\omega_o/\omega - \omega/\omega_o\right)^2}$$

where T is the transmission power and is equal to the power delivered through the resonator divided by the incident power. By measuring near the resonant frequency, the frequency terms cancel. The assumption of $Q_E = Q_{E'}$ can be made since both external lines are identical and should give the same losses. The insertion loss, IL, can be measured, and is related to T by:

$$IL = 10 Log_{10}(T)$$

From this, the corrected Q is shown to be:

$$Q_U = \frac{Q_L}{1 - Log_{10}^{-1}\left(\frac{IL}{20}\right)}$$

The surface resistance of the superconductor was calculated by comparing its Q with that of a copper sample, which has a known surface resistance.

$$R_{sc} = \left(\frac{Q_{Cu'}}{Q_{SC}}\right) R_{Cu}$$

where Q_{SC} is the corrected Q measured from the superconducting fiber, and $Q_{Cu'}$ is the Q of a copper wire of similar dimensions in the same cavity. The surface resistance of copper, R_{Cu}, is taken to be 3.30×10^{-3} [31].

$$Q_{Cu'} = Q_{Cu}\sqrt{\frac{f_{SC}}{f_{Cu}}} \times \frac{\text{superconductor fiber diameter}}{\text{copper wire diameter}}$$

where f_{SC} and f_{Cu} are the frequencies at which the Q was measured for the superconductor and copper wire respectively. The measured Q_{Cu} in the cavity used was 1557 at 77 K and 805.7 MHz.

The rf field strength will vary along the conductor, with the maximum field, $H_{rf,max}$, at the node of the the resonating wave. This is calculated by [28]:

$$H_{rf,max} = \frac{I_{rf}}{2\pi a} \times \left(0.01256637 \ \frac{\text{Oe}}{\text{A/m}}\right) \quad \text{(in Oe)}$$

where a is the fiber radius, and the radio frequency surface current I_{rf} is

$$I_{rf} = \sqrt{\frac{r_v(1-r_v)8QP}{n\pi Z_0}}$$

$$r_v = Log_{10}^{-1}\left(\frac{\text{Insertion Loss}}{\text{-20}}\right)$$

$$P = \left[Log_{10}^{-1}\left(\frac{dBm}{10}\right)\right] \times 10^{-3} \quad \text{(watts)}$$

and [32]

$$Z_0 = \frac{60}{\sqrt{\varepsilon_r}} \ln\left(\frac{b}{a}\right) \ (\Omega)$$

$$\varepsilon_r = 1.454$$

B. R_s vs H_{rf} Dependence

Sample # F269

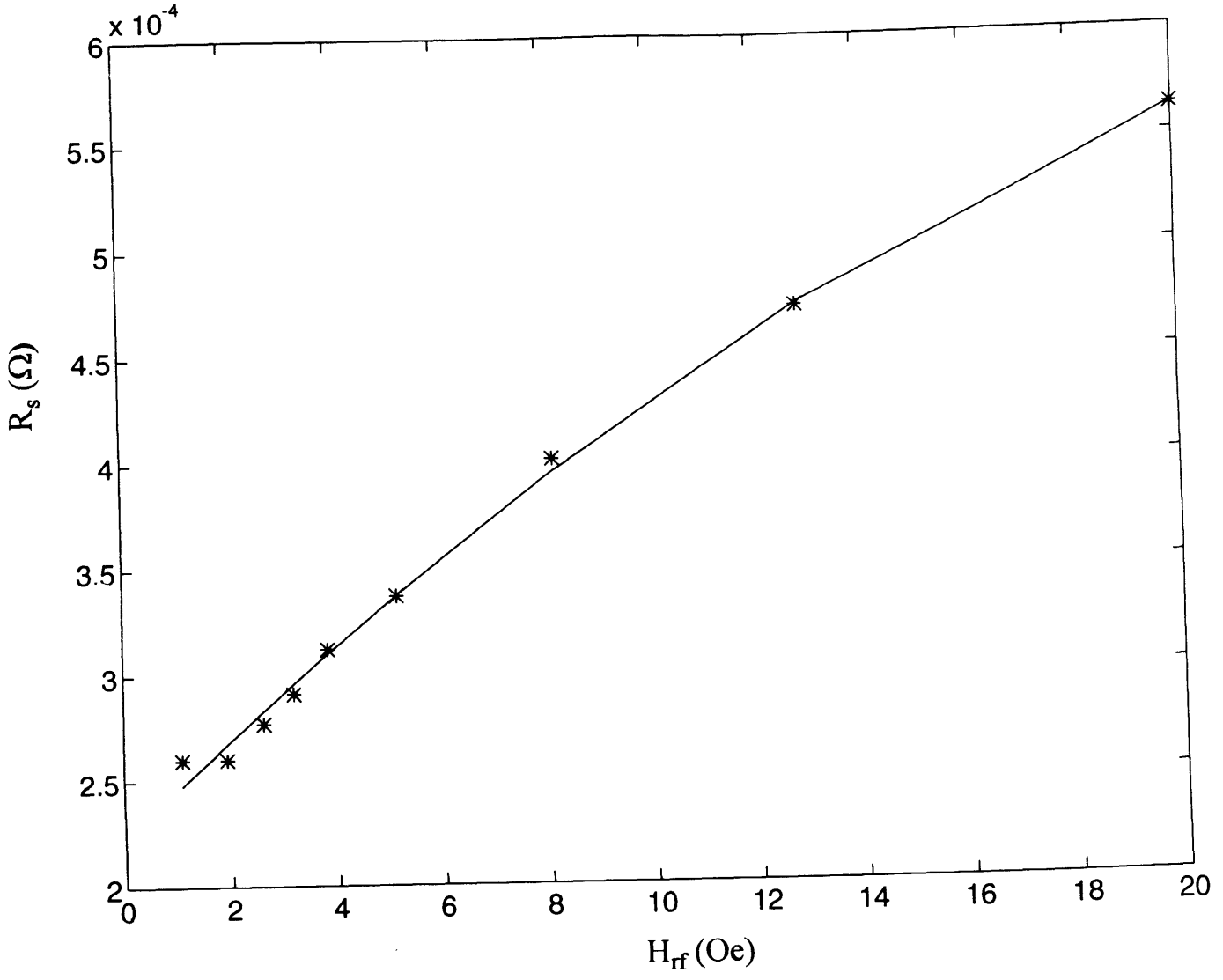

Sample # F2721

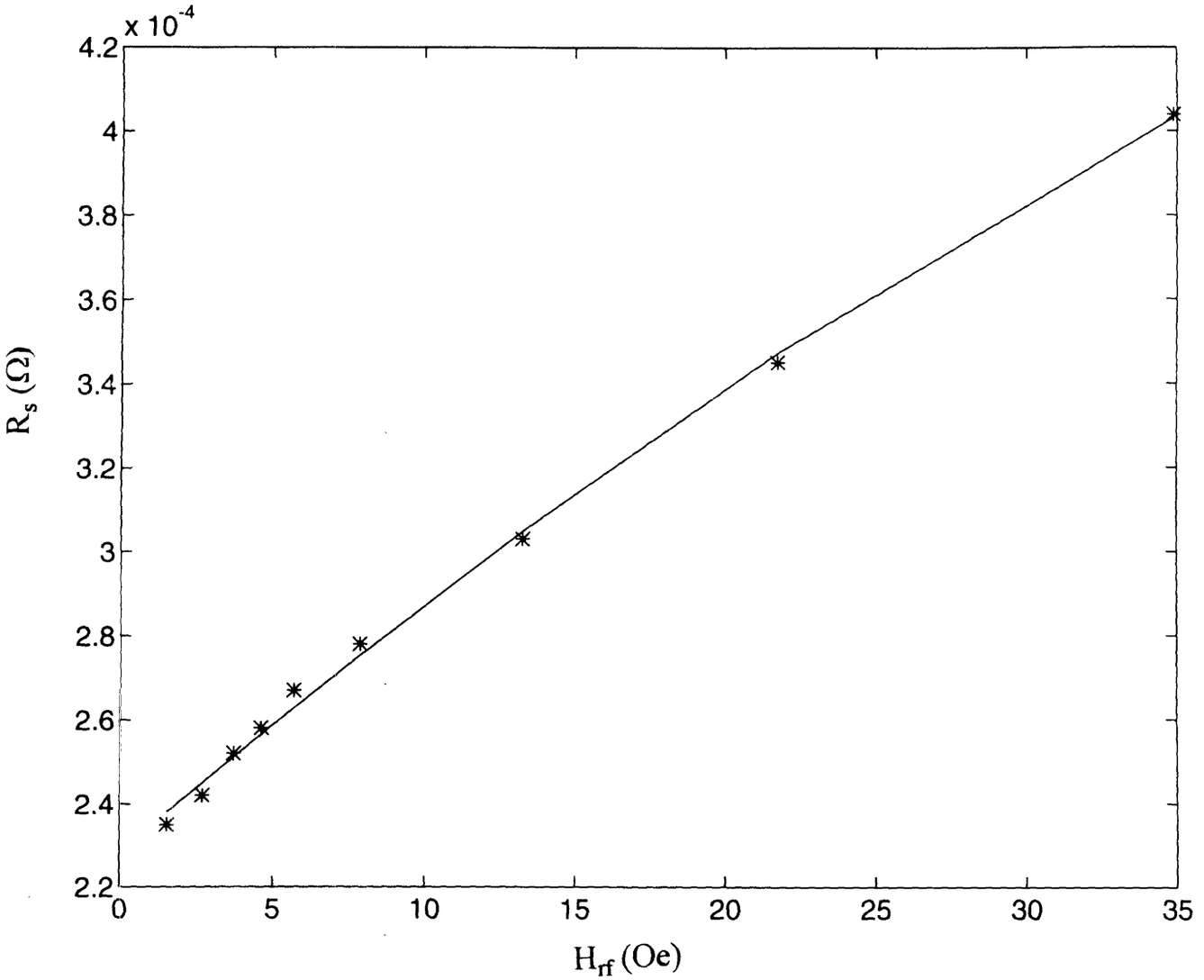

Sample # F3721

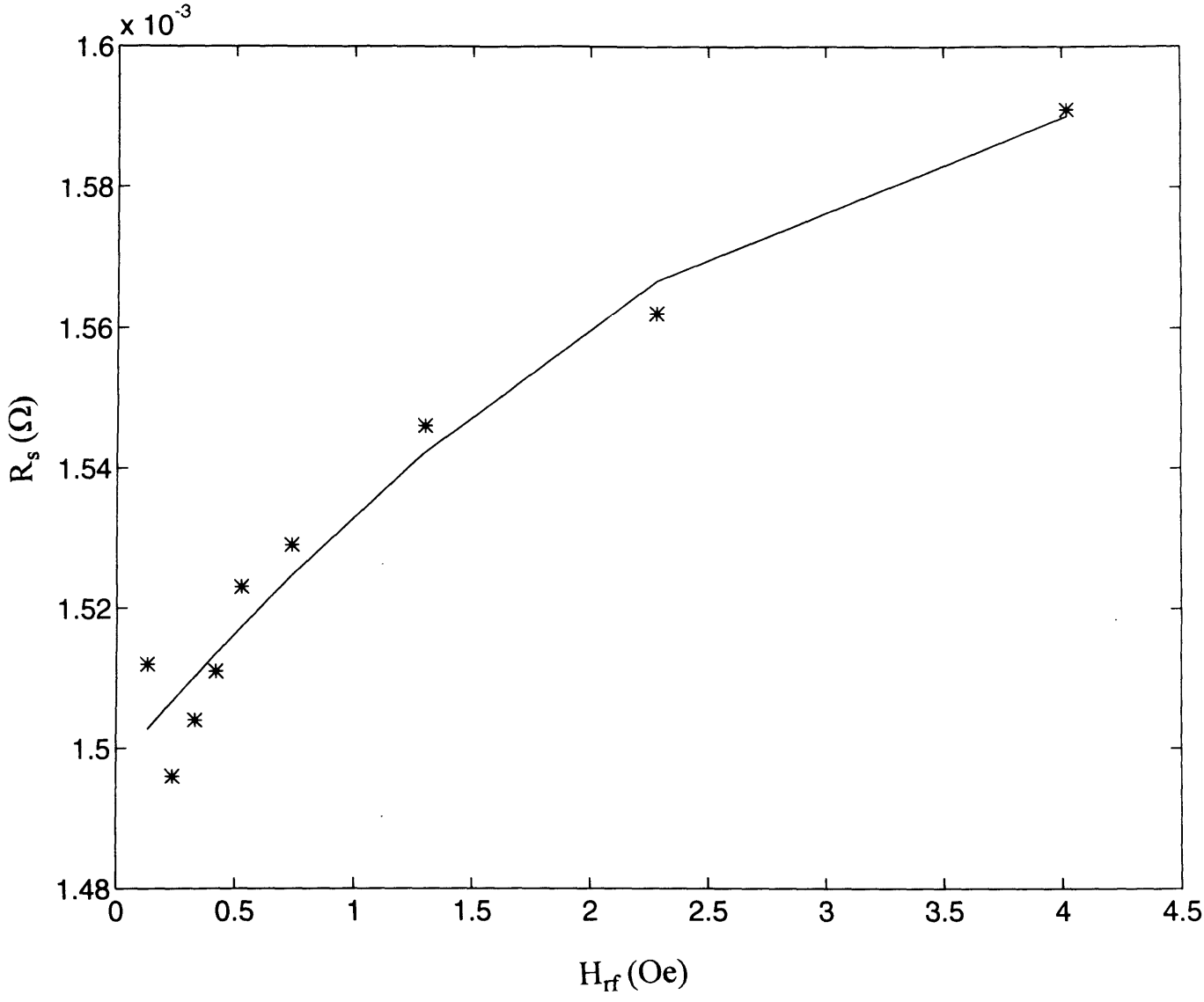

Sample # F3726

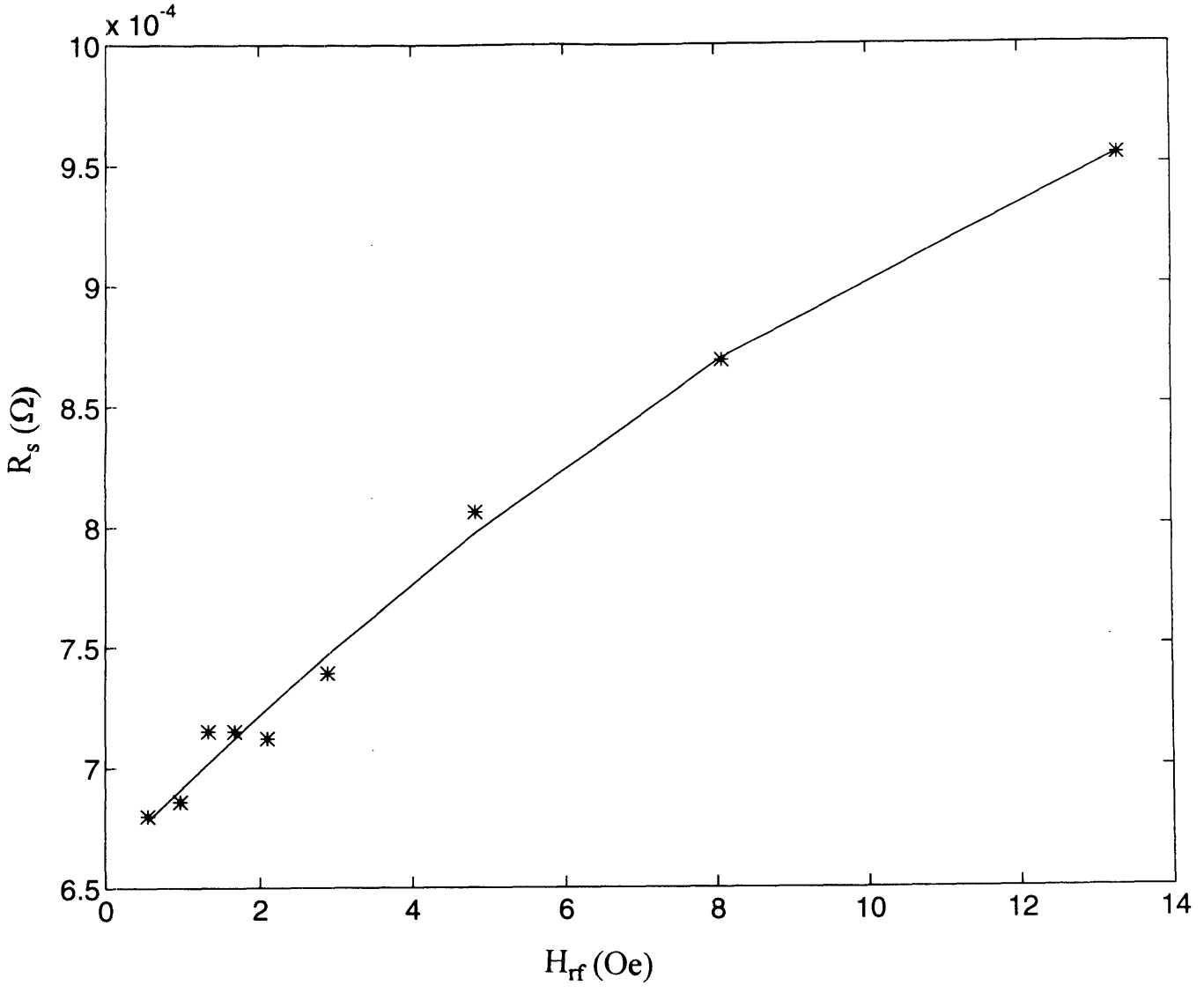

Sample # F3729

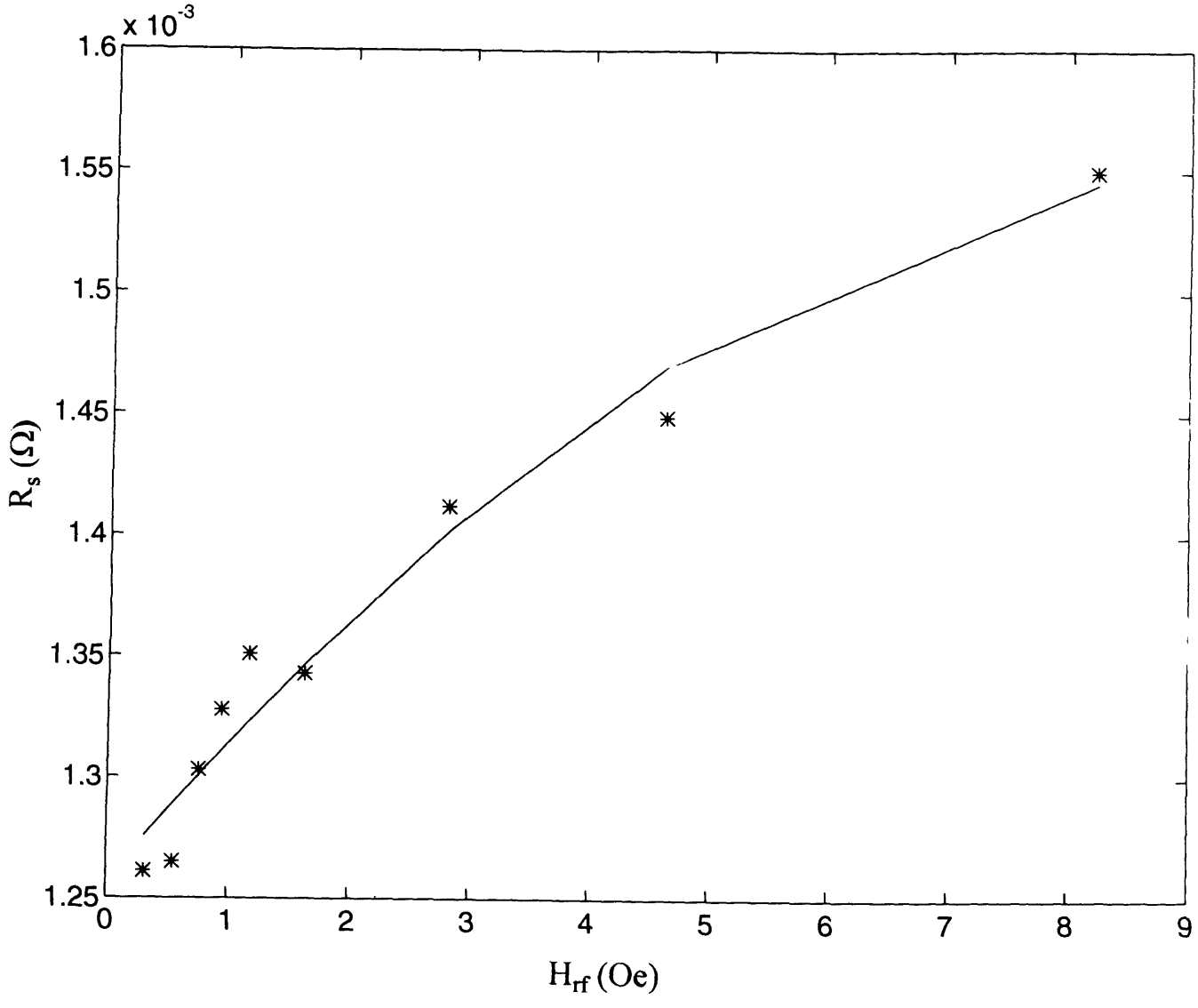

Sample # F4611

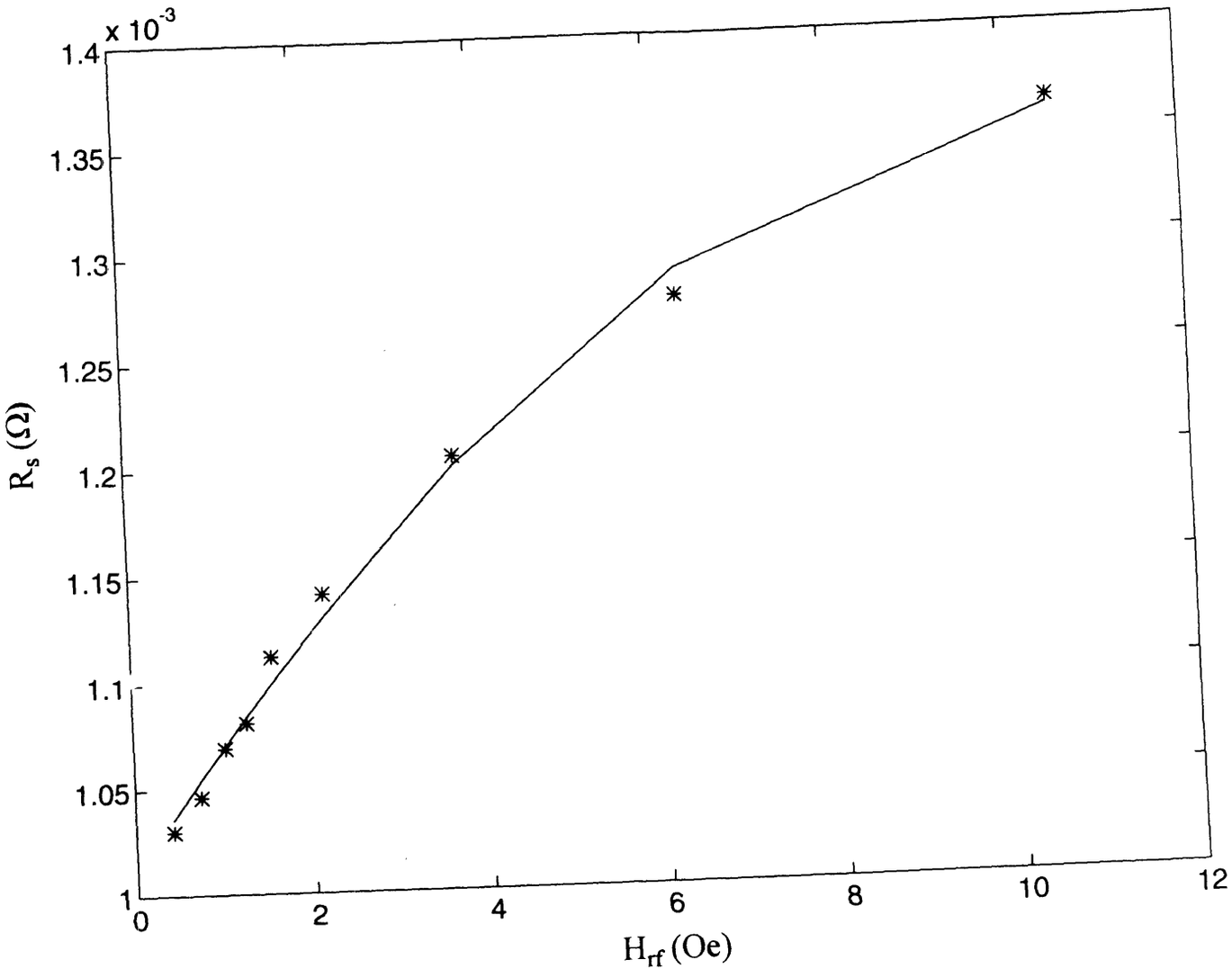

Sample # F4618

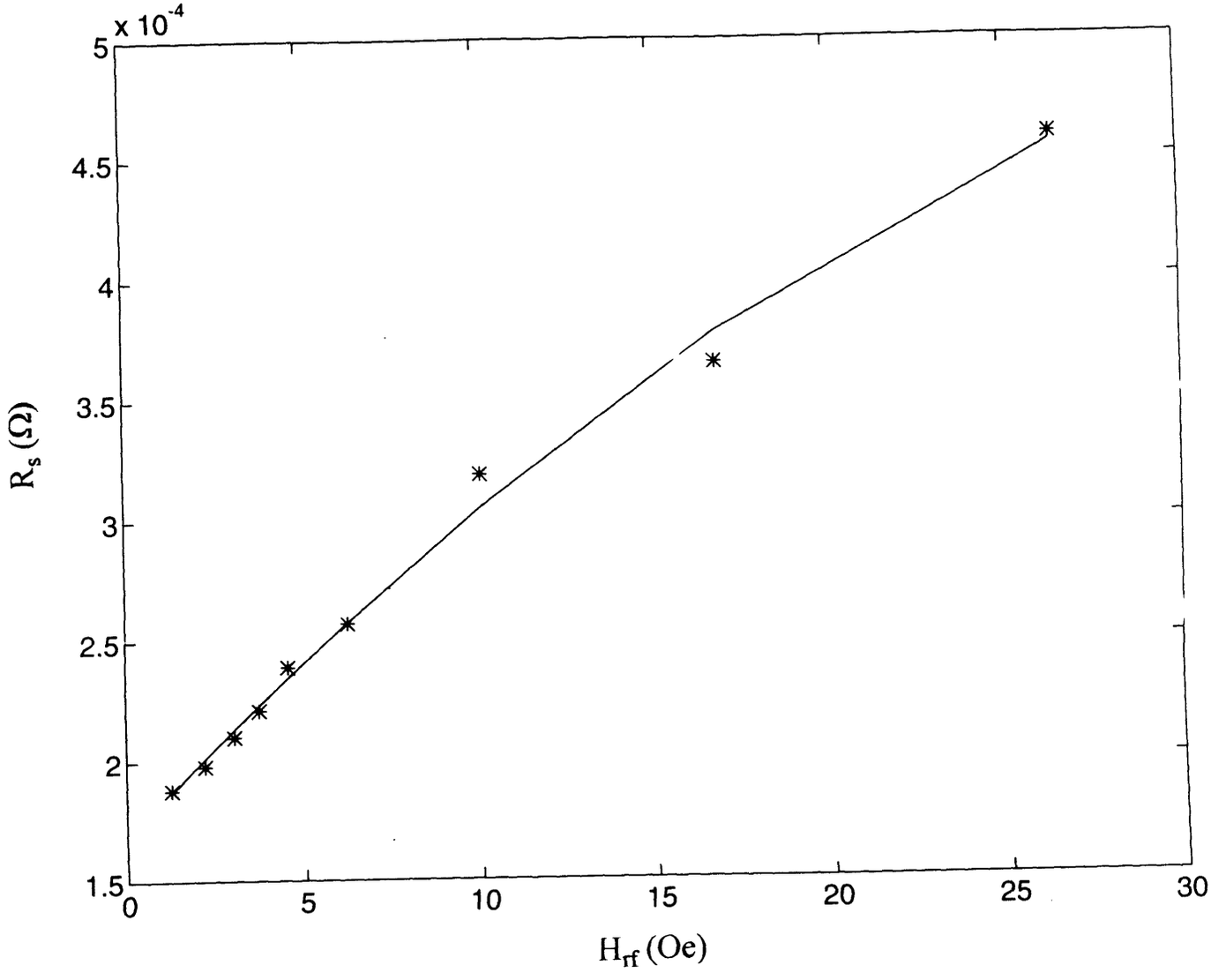

Sample # F4719 (at 2nd harmonic frequency)

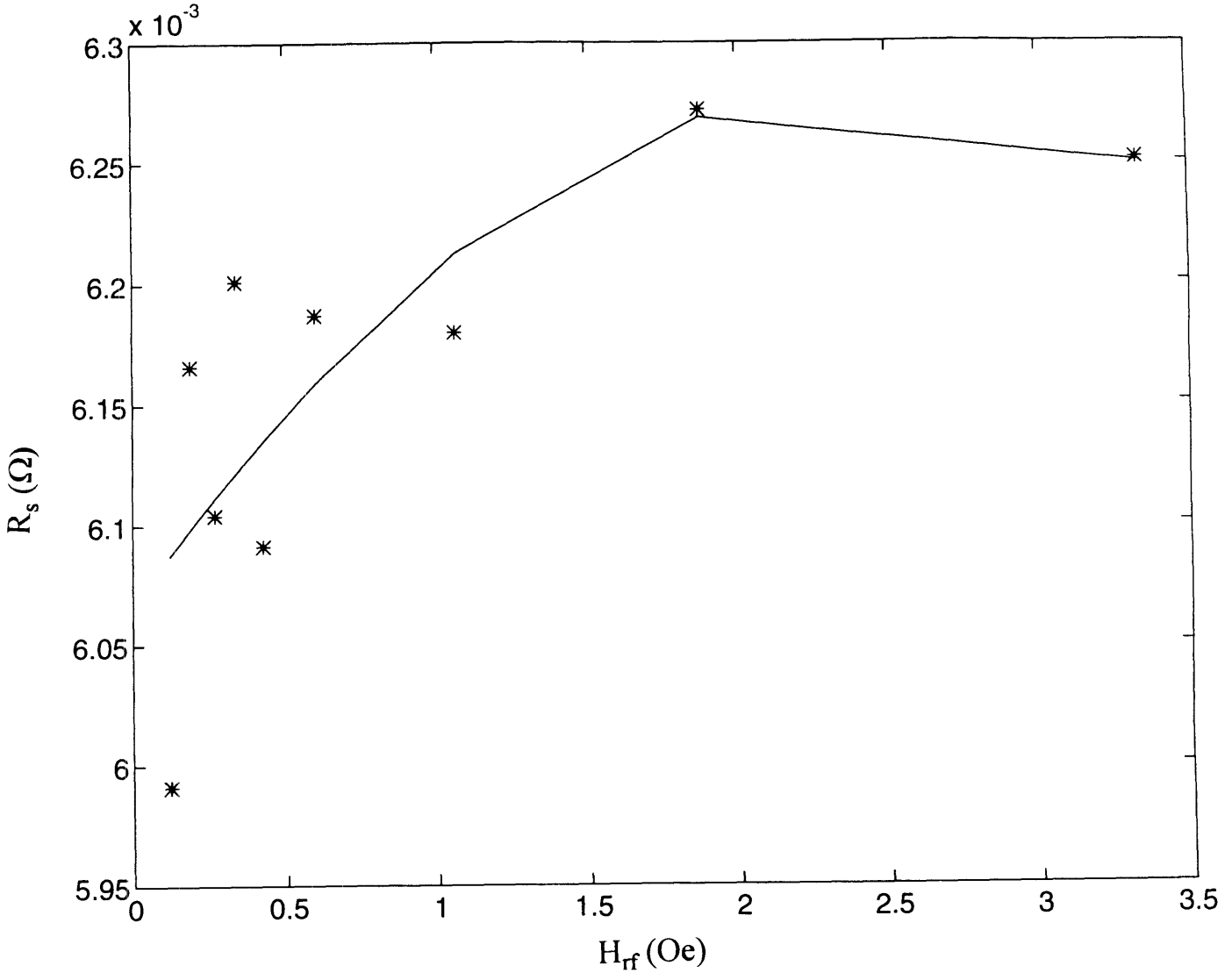

Sample # F4719 (at 3rd harmonic frequency)

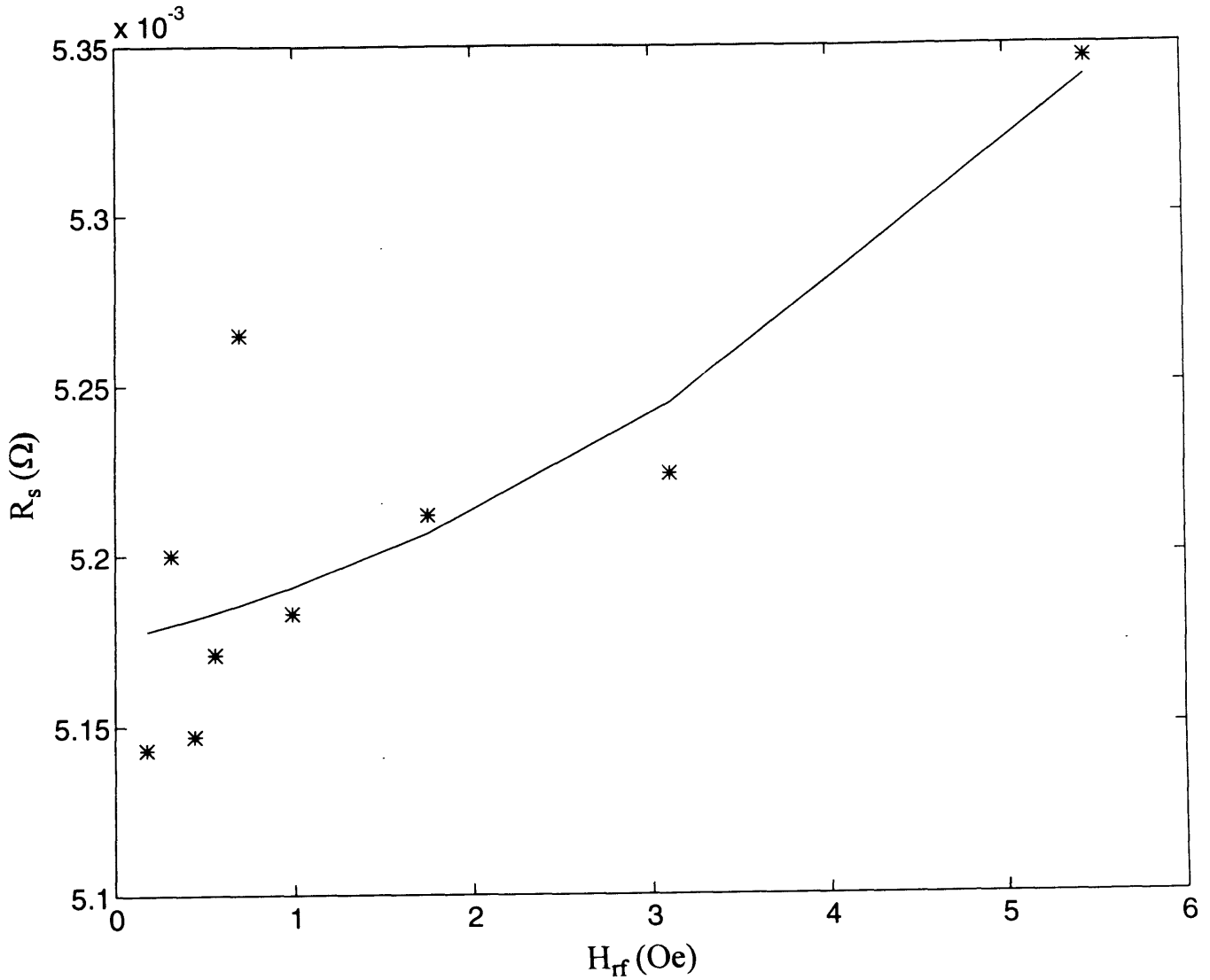

Sample # F4726

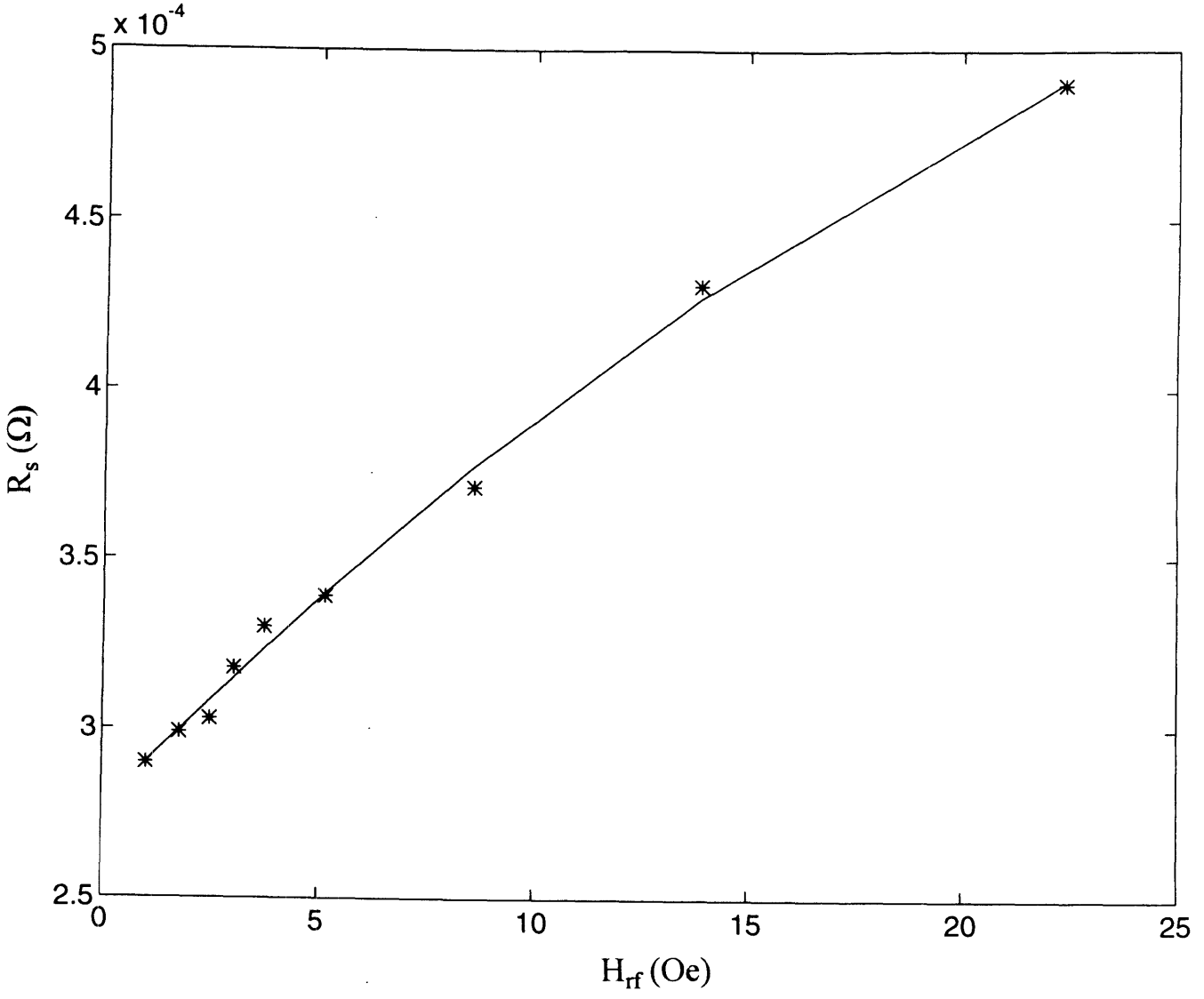

Sample # F4726 (at 2nd harmonic frequency)

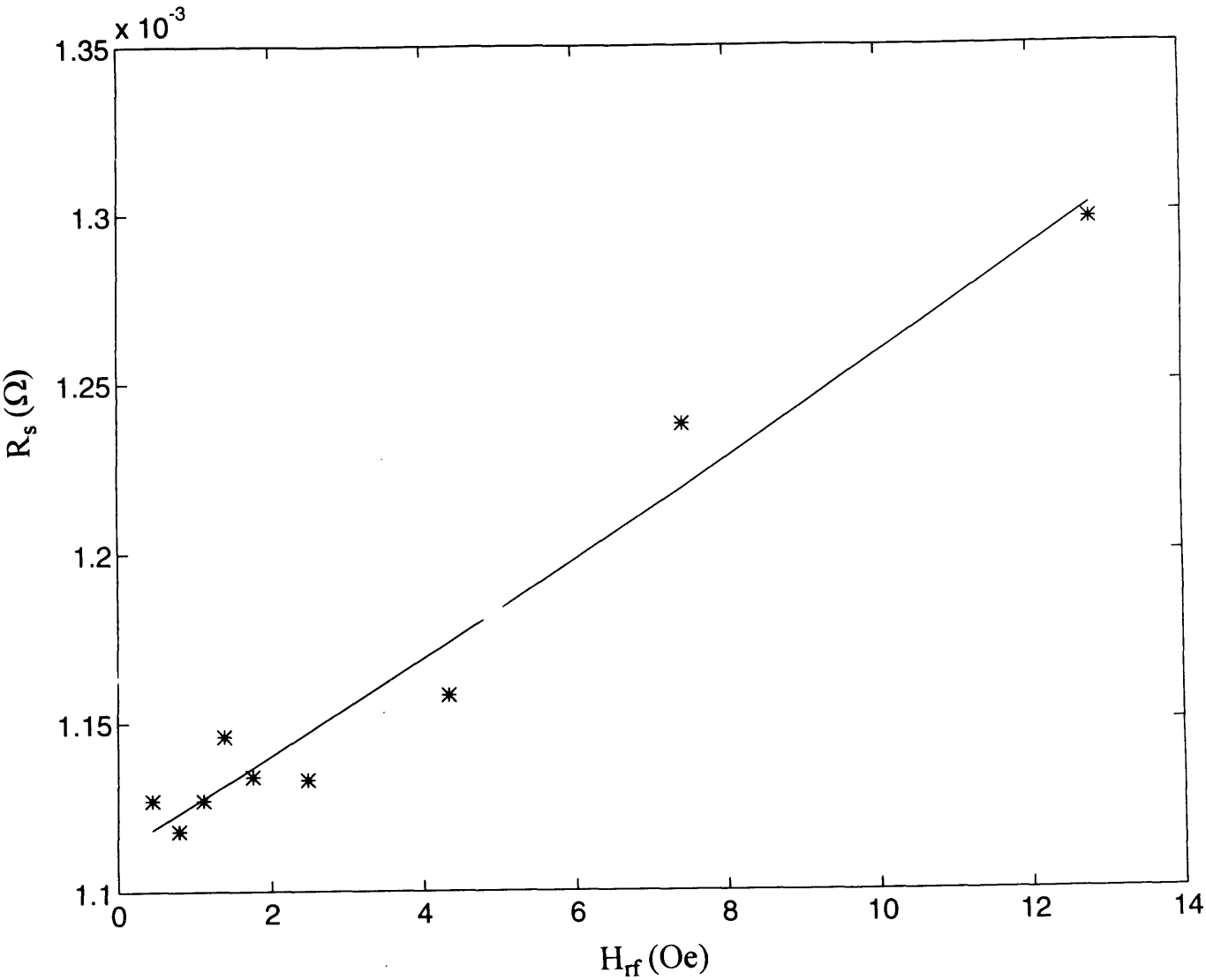

Sample # FE12-15

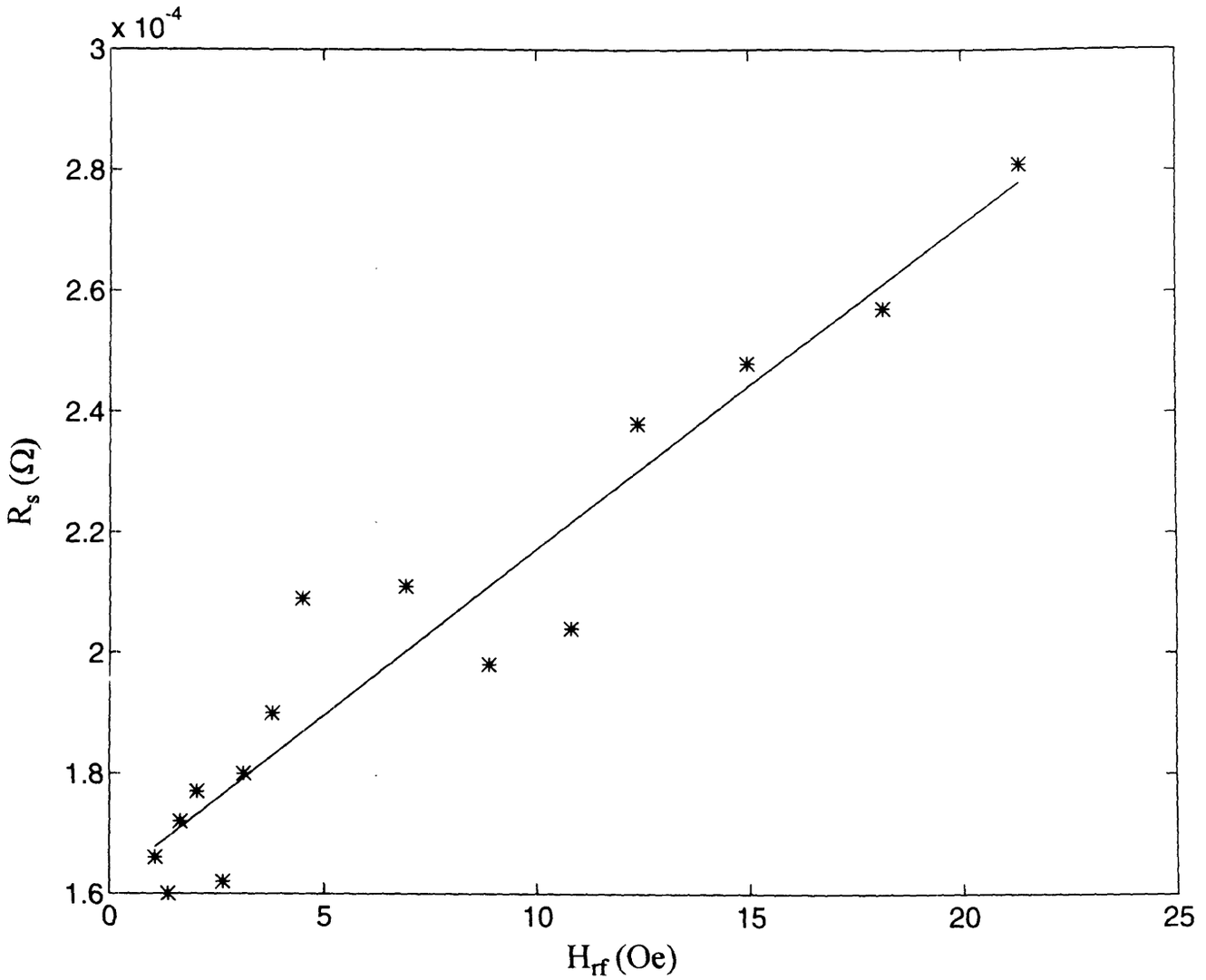

Sample # FE12-15 (at 2nd harmonic frequency)

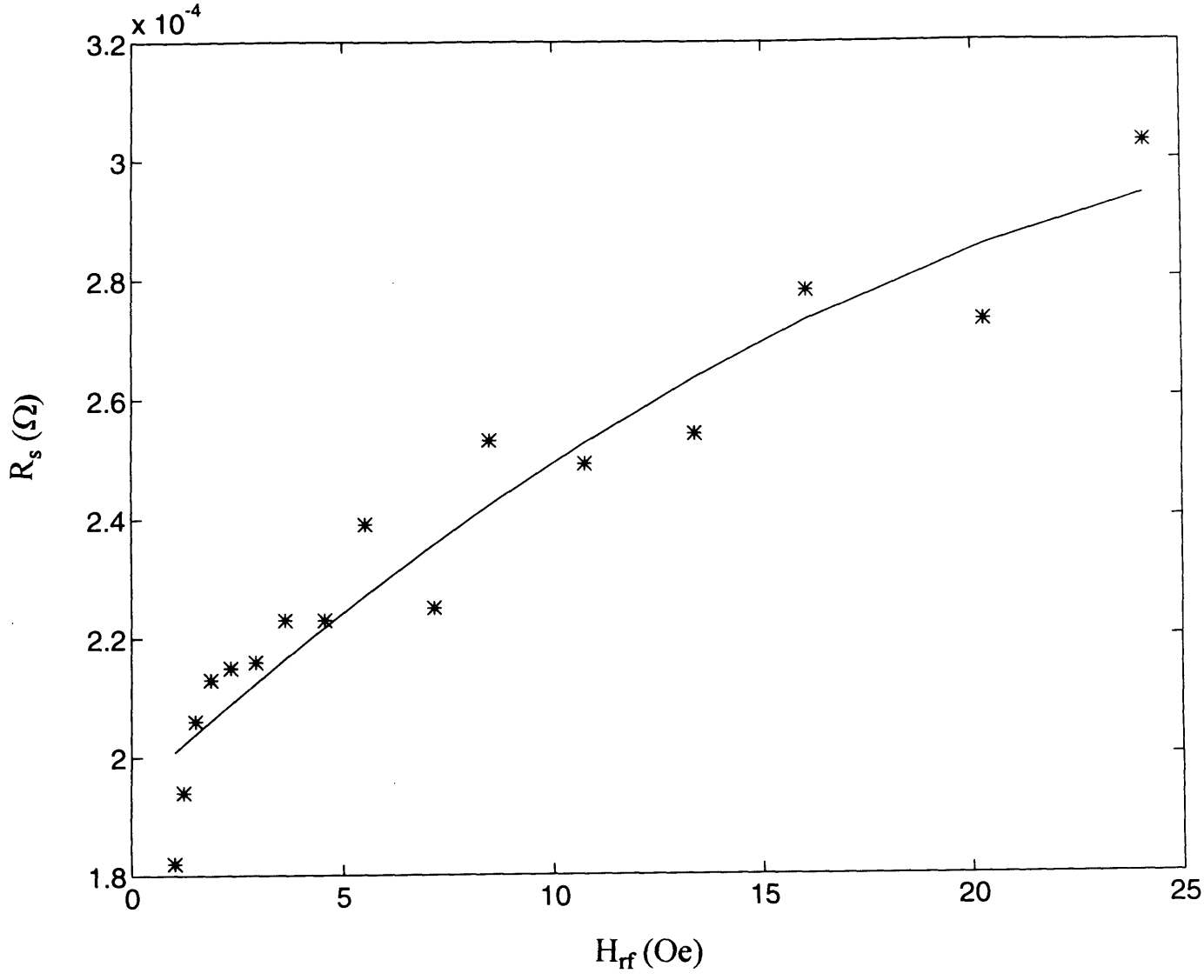

IX. Bibliography

1. A. C. Rose-Innes and E. H. Rhoderick, Introduction to Superconductivity, 2nd ed. Pergamon, Inc. 1978.

2. D. R. Tilley and J. Tilley, Superfluidity and Superconductivity. 2nd ed., Adam Hilger Ltd 1986.

3. A. Goyal, K. B. Alexander, D. M. Kroeger, P. D. Funkenbusch, and S. J. Burns, "Solidification of $YBa_2Cu_3O_{7-\delta}$ From the Melt", *Physica C* **210** p197-212 (1993).

4. R. Pragasam, C. Srinivasan, V. R. K. Murthy, B. Viswanathan, J. Sobhanadri, K. M. Satyalakshmi, and M. S. Hegde, "Comparison of the effect of processing parameters and degradation on the DC and microwave properties of thin films and polycrystalline bulk high-Tc superconducting materials", *Superconductor Science and Technology* **6** (1993) 402-407.

5. C. C. Chin, P. J. Rainvill, A. J. Drehman, J. S. Derov, J. Steinbeck, G. Dresselhaus, and M. S. Dresselhaus, "Surface resistance measurement of superconducting $YBa_2Cu_3O_7$ in a magnetic field", *Journal of Materials Research* **5** (1990) 1599-1604.

6. R. Reed-Hill and R. Abbashian, Physical Metallurgy Principles 3rd ed., PWS-KENT Publishing Co. (1992).

7. A. Goyal, P. D. Funkenbusch, D M. Kroeger, S. J. Burns, "Anisotropic Hardness and Fracture-Toughness of Highly Aligned $YBa_2Cu_3O_{7-\delta}$", *Journal of Applied Physics* **71** 2363 (1991).

8. P. K. Gallagher, H. M. O'Bryan, S. A. Sunshine, and D. W. Murphy, "Oxygen stoichiometry in $Ba_2YCu_3O_x$", *Materials Research Bulletin* **22** 995-1006 (1987).

9. M. J. Cima, M. C. Flemings, A. M. Figueredo, M. Nakade, H. Ishii, H. D. Brody, and J. S. Haggerty, "Semisolid solidification of high temperature superconducting oxides", *Journal of Applied Physics* **72** 179-190 (1992).

10. S. Nakahara, G. J. Fisanick, M. F. Yan, R. B. Vandover, T. Boone, and R. Moore, " On the Defect Structure of Grain-Boundaries in $Ba_2YCu_3O_{7-x}$", *Journal of Crystal Growth* **85** (1987) 639-651.

11. T. K. Worthington, W. J. Gallagher, and T. R. Dinger, "Anisotropic Nature of High-Temperature Superconductivity in Single-Crystal $YBa_2Cu_3O_{7-x}$", *Physical Review Letters* **59** (1987) 1160-1163.

12. A. P. Malozemoff, T. K. Worthington, Y. Yeshurun, F. Holtzberg, and P. H. Kes, "Frequency dependence of the ac susceptibility in a Y-Ba-Cu-O crystal: A reinterpretation of H_{c2}", *Physical Review B* **38** (1988) 7203-7206.

13. W. W. Macalpine and R. O. Schildknecht, "Coaxial Resonators with Helical Inner Conductor", *Proceedings of the IRE* (1959) 2099-2105.

14. D. J. Miley and J. B. Beyer, "Field Analysis of Helical Resonators with Constant-Bandwidth Filter Application", *IEEE Transactions on Parts, Materials and Packaging* **PMP-5** (1969) 127-132.

15. D. R. Bowling, R. J. Dinger, and N. M. Alford, "Surface Resistance Measurements of Superconducting YBCO Helices at UHF".

16. C. W. Lam, D. M. Sheen, S. M. Ali, and D. E. Oates, "Modeling the Nonlinearity of Superconducting Strip Transmission Lines", *IEEE Transactions on Applied Superconductivity* **2** (1992) 58-65.

17. D. E. Oates, A. C. Anderson, D. M. Sheen, and S. M. Ali, "Stripline Resonator Measurements of Zs Versus H_{rf} in $YBa_2Cu_3O_{7-x}$ Thin Films", *IEEE Transactions on Microwave Theory and Techniques* **39** (1991) 1522-1529.

18. Z. L. Wang, A. Goyal, and D. M. Kroeger, "Structural and chemical disorder near the $Y_2BaCuO_5/YBa_2Cu_3O_{7-\delta}$ interface and its possible relation to the flux-pinning behavior in melt-textured $YBa_2Cu_3O_{7-\delta}$", *Physical Review B* **47** 5373-5382.

19. A. S. Parikh, B. Meyer, and K. Salama, "A Method to Improve Grain Boundary Current Carrying Capability in Melt Textured YBCO", (To be published).

20. S. Jin, "Texturing and Flux Pinning in High Tc Superconductors", High Temperature Superconducting Compounds III, ed. S.Whang, A DasGupta, and E. Collings The Minerals, Metals and Materials Society (1991) 67-77.

21. H. Teshima, "Review of QMG materials", Presentation viewgraphs at a seminar held 8/16/93.

22. H. S. Horowitz, R. K. Bordia, R. B. Flippen, and R. E. Johnson, "Effect of Ambient Atmosphere on $YBa_2Cu_3O_{7-y}$", *Materials Research Society Symposium Proceedings* **99** (1988) 903-906.

23. J. Halbritter, "On Intrinsic and Extrinsic Effects in the Surface Impedance of Cuprate Superconductors", *Journal of Superconductivity* **5** (1992) 331-337.

24. A. M. Portis, "Microwave Power-Induced Flux Penetration and Loss in High-Temperature Superconductors", *Journal of Superconductivity* **5** (1992) 319-330.

25. A. M. Portis, D. W. Cooke, and E. R. Gray, "RF Properties of High-Temperature Superconductors: Cavity Methods", *Journal of Superconductivity* **3** (1990) 297-304.

26. H. A. Blackstead, D. B. Pulling, P. J. McGinn, and W. H. Chen, "Twin-Boundary Pinning and Flux Flow in Zone-Melting $YBa_2Cu_3O_{7-\delta}$ Crystals", *Journal of Superconductivity* **4** (1991) 263-269.

27. D. E. Oates, A. C. Anderson, and P. M. Mankiewich, "Measurement of Surface Resistance of
$YBa_2Cu_3O_{7-x}$", *Journal of Superconductivity* **3** (1990) 251-259.

28. M. Cima, discussion 1/18/94.

29. L. Solymar and D. Walsh, "Lectures on the Electrical Properties of Materials", Fourth Ed., Oxford University Press, (1988).

30. M. Hein, F. Hill, G. Muller, H. Piel, H. P. Schneider and M. Strupp, "Potential of Polycrystalline YBCO Layers for Applications", *IEEE Transactions on Applied Superconductivity* **3** #1 (1993) 1745-1748.

31. S. Ramo, J. R. Whinnery, and T. Van Duzer, Fields and Waves in Communication Electronics, John Wiley (1965) p252.

32. N. Marcuvitz, Waveguide Handbook, McGraw-Hill, New York (1951).

33. J. Delayen, K. Goretta, R. Poeppel and K. Shepard, "RF Properties of an Oxide-Superconductor Half-wave Resonant Line," *Applied Physics Letters* **52** #11 (1988) p 930-32.

34. J. Delayen and C. Bohn, "Temperature, Frequency, and RF Field Dependence of the Surface Resistance of Polycrystalline $YBa_2Cu_3O_{7-x}$," *Physical Review B* **40** #7 (1989) p5151-54.

35. N. Klein, U. Poppe, N. Tellmann, H. Schulz, W. Evers, U. Dahne and K. Urban, "Microwave Surface Resistance of Epitaxial YBa2Cu3O7-x Films: Studies on Oxygen Deficiency and Disordering," *IEEE Transactions on Applied Superconductivity*, **3** #1 (1993) p1102-9.

Biographical Note

Michael Daniels attended M.I.T. from 1989-1994. He received his B.S. degree in May 1993 and went on to complete his M.S. in May 1994, with both degrees being in Materials Science and Engineering. He is also a member of Sigma Xi.

5838-15